

Hot phase generation by supernovae: resolution, chemistry and thermal conduction

Ulrich P. Steinwandel,^{1,2*}† Benjamin P. Moster,^{1,2}, Thorsten Naab², Chia-Yu Hu³ and Stefanie Walch⁴

¹Universitäts-Sternwarte München, Fakultät für Physik, LMU Munich, Scheinerstr. 1, 81679, Germany

²Max Planck Institute for Astrophysics, Karl-Schwarzschild-Str. 1, 85748, Garching, Germany

³Center for Computational Astrophysics, Flatiron Institute, 162 5th Ave NY NY, USA

⁴Physikalisches Institut der Universität zu Köln, Zùlpicher Strasse 77, 50937 Köln, Germany

Accepted XXX. Received YYY; in original form ZZZ

ABSTRACT

Supernovae (SN) generate hot gas in the interstellar medium (ISM), help setting the ISM structure and support the driving of outflows. It is important to resolve the hot gas generation for galaxy formation simulations at solar mass and sub-parsec resolution which realise individual supernova (SN) explosions with ambient densities varying by several orders of magnitude in a realistic multi-phase ISM. We test resolution requirements by simulating SN blast waves at three metallicities ($Z = 0.01, 0.1$ and $1Z_{\odot}$), six densities and their respective equilibrium chemical compositions ($n = 0.001 \text{ cm}^{-3} - 100 \text{ cm}^{-3}$), and four mass resolutions ($0.1 - 100 M_{\odot}$). We include non-equilibrium cooling and chemistry, a homogenous interstellar radiation field, and shielding with a modern pressure-energy smoothed particle hydrodynamics (SPH) method including isotropic thermal conduction and a meshless-finite-mass (MFM) solver. We find stronger resolution requirements for chemistry and hot phase generation than for momentum generation. While at $10 M_{\odot}$ the radial momenta at the end of the Sedov phase start converging, the hot phase generation and chemistry require higher resolutions to represent the neutral to ionised hydrogen fraction at the end of the Sedov phase correctly. Thermal conduction typically reduces the hot phase by 0.2 dex and has little impact on the chemical composition. In general, our 1, and $0.1 M_{\odot}$ results agree well with previous numerical and analytic estimates. We conclude that for the thermal energy injection SN model presented here resolutions higher than $10 M_{\odot}$ are required to model the chemistry, momentum and hot phase generation in a multi-phase ISM.

Key words: methods: numerical – galaxies: formation – galaxies: ISM – ISM: supernova-remnants – ISM: structure – ISM: abundances

1 INTRODUCTION

The galactic interstellar medium is shaped by the feedback of massive stars. A physical process which is of paramount importance in this picture are SN-explosions. Core-collapse-supernovae (SNe) eject gas at supersonic velocities of several thousand kilometres per second (e.g. Blondin et al. 1998; Janka et al. 2012) and drive blast waves into the ISM. The evolution of SN-remnants has been extensively investigated analytically, and can be divided in four phases (e.g. Woltjer 1972): the phase of ‘free-expansion’ which is terminated when the swept up mass equals the ejecta mass (roughly

a few 100 years), the energy conserving Sedov-Taylor (ST) phase (e.g. Sedov 1946, 1959; Taylor 1950), the pressure driven (PDS) phase and the momentum conserving snow plough phase (MCS; Falle 1975). In the PDS-phase the pressure of the bubble interior further generates momentum until pressure equilibrium with the shell is reached and the bubble evolves the remnant in the low pressure regime (Cox 1972; Gaffet 1983; Cioffi et al. 1988; Cohen et al. 1998; Haid et al. 2016). In the MCS-phase the momentum of the shell is conserved and the further evolution of the shell is driven by the generated inertia of the swept up mass (Cioffi et al. 1988; Haid et al. 2016). The energy conserving ST-phase is of particular importance as it is the main momentum generating phase with an expanding hot bubble. This momentum build up due the ST-phase drives turbulence within the ISM and

* E-mail: usteinw@usm.lmu.de

† E-mail: uli@mpa-garching.mpg.de

regulates star formation within galaxies. It can last from a few 1000 years in dense environments to several Myr in low density environments. The duration of the ST-phase is highly dependent on the cooling properties of the ambient ISM. In this phase the SN-remnant behaves adiabatically because there are (nearly) no cooling losses that can remove energy from the system.

Blast waves replenish the hot phase of the ISM (Cox & Smith 1974; McKee & Ostriker 1977) through shocks (e.g. Gottthelf et al. 2001), generate momentum and build up turbulence (Elmegreen & Scalo 2004; Scalo & Elmegreen 2004) in the warm neutral medium (WNM) of the ISM (Mac Low & Klessen 2004). The hot phase generated by SNe fills a large fraction of the turbulent ISM volume (e.g. McKee & Ostriker 1977; Ferrière 1998; Könyves et al. 2007) in which smaller and cooler clouds are embedded, as observed in the local ISM (e.g. Frisch et al. 2011). SNe also enrich the ISM with metals and dust (e.g. Dwek 1998; Indebetouw et al. 2014; Kobayashi et al. 2011; Matsuura et al. 2011), different atomic species, and form molecules in their remnants (Spyromilio et al. 1988; Grefenstette et al. 2014; Fransson et al. 2016; Kamenetzky et al. 2013). When multiple SNe occur in a low density environment, subsequent explosion add mass to the shell and heat the interior of the bubble which can lead to the formation of ‘super-bubbles’ (Castor et al. 1975; Weaver et al. 1977; McCray & Kafatos 1987; Tomisaka & Ikeuchi 1986; Mac Low & McCray 1988; Koo & McKee 1992). These can drive strong galactic outflows which redistribute the gas on galactic scales and moves a fraction of it towards the circum galactic medium (CGM) of the galaxy. In more general terms, the feedback from SNe can regulate the cosmic baryon cycle and the star formation rate (SFR) of galaxies across cosmic time (c.f. Somerville & Davé 2015; Naab & Ostriker 2017).

In cosmological simulations of galaxy formation, stellar feedback leads to a better agreement with the properties of the observed stellar and gaseous components, such as the low conversion efficiency of gas into stars which are determined empirically (e.g. Moster et al. 2010; Behroozi et al. 2010; Moster et al. 2013) and disk-like galaxy morphologies (Naab & Ostriker 2017; Somerville & Davé 2015). However, most simulation cannot resolve the momentum and hot medium generating phases of blast waves and fall back on “sub-resolution” implementations to mimic the SN impact. Simulations adopting these methods have been able to produce galaxy morphology and population properties in agreement with observations (e.g. Guedes et al. 2011; Aumer & White 2013; Marinacci et al. 2014; Agertz et al. 2013; Wang et al. 2015; Hopkins et al. 2018), and empirical predictions (e.g. Moster et al. 2018; Behroozi et al. 2018). However, it remains unclear how well the underlying physical processes are really captured, and to what degree these results are achieved by fine-tuning model parameters.

Recently, it has become possible to simulate low mass galactic systems like dwarf galaxies at such high resolution that the impact of supernovae from individual massive stars can be accurately captured in the relevant temperature and density regimes of the multi-phase ISM (Forbes et al. 2016; Hu et al. 2016; Emerick et al. 2019). This approach, however, requires a detailed understanding of the resolution requirements for resolving individual blast waves in the turbulent cold, warm and hot ISM. Many high-resolution simulations

of SN blast waves in ambient homogeneous media or turbulent ISM patches have been carried out to understand their evolution in detail (e.g. Ostriker & McKee 1988; Blondin et al. 1998; Thornton et al. 1998; Draine 2011; Kim & Ostriker 2015; Walch et al. 2015; Gatto et al. 2015; Martizzi et al. 2015; Haid et al. 2016; Ohlin et al. 2019). Apart from emerging resolution requirements, it has become clear that the distribution of ambient densities of SN blast waves play an important role for how efficiently they can drive turbulence and outflows (Girichidis et al. 2016; Hu et al. 2016, 2017; Gatto et al. 2017; Naab & Ostriker 2017; Seifried et al. 2018). While the turbulent component of the ISM can be generated by adopting some feedback prescription that injects the momentum of SNe, the galactic winds are driven by the pressure that is generated by the SNe within the turbulent ISM. In simulations, many factors like spatial resolution, stellar winds, radiation, SN clustering and binary or runaway stars can affect the ambient SN density distributions (Kim et al. 2017; Gentry et al. 2017; Naab & Ostriker 2017; Peters et al. 2017; Fielding et al. 2018). However, not only numerical implementation, resolution constraints and ambient density distribution of blast waves determine their impact but also the complexity of the physical modelling. For example magnetic fields, cosmic rays (e.g. Diesing & Caprioli 2018; Gupta et al. 2018) and thermal conduction (e.g. Keller et al. 2014; El-Badry et al. 2019) change their evolution.

In this paper we use two particle based hydrodynamical methods: modern smoothed particle hydrodynamics (SPH) and the meshless finite mass (MFM) method (Gaburov & Nitadori 2011; Hopkins 2015). We couple both solvers to a non-equilibrium chemical network to estimate their ability to converge on blast wave evolution in cold, warm and hot ambient media at different numerical resolutions. Furthermore we use the SPH implementation to probe the impact of thermal conduction on individual blast waves. This study is also the numerical basis for galaxy scale simulations which have been and will be carried out at solar mass and sub-parsec resolution. The paper is structured as follows. In section 2 we briefly present the numerical and physical methods that are important for this study and discuss the simulation setup and the initial parameters that are important for our cooling and chemistry network. In section 3 we discuss our results for isolated SNe blast waves in a homogeneous medium (e.g. structure of the blast wave its environmental dependence). In section 4 we use the physical properties from our simulations to constrain the expectation value for a hot phase to form as a function of their environmental densities. In section 5 we discuss the effect of isotropic heat conduction on the SN-remnant evolution in our highest resolution runs. Finally, we summarise our results in section 6.

2 SIMULATION METHOD

2.1 Hydrodynamics

We run our set of simulations with our version of Gadget-3 (Springel 2005), which includes implementations for several hydrodynamics solvers, such as pressure-energy SPH (Hu et al. 2014) and the meshless finite mass (MFM) (e.g. Gaburov & Nitadori 2011; Hopkins 2015). In Hu et al. (2014)

it is shown that the improved pressure-energy SPH accurately captures shocks and instabilities in several idealised test problems. While MFM shares the kernel weighted density computation with SPH, the hydrodynamical flux vectors are integrated over the one-dimensional Riemann-problem defined on the surface between two reconstruction points of the fluid equations (particles). In combination with a second order reconstruction of the flux gradients (Gaburov & Nitadori 2011; Mocz et al. 2014) it is possible to obtain a second order hydrodynamical scheme with an appropriate mathematical consistency and convergence proof as shown in Lanson & Vila (2008). We follow the slope limiting and reconstruction procedures by Hopkins (2015). We calculate the quadrature point in first order via $\mathbf{x}_{ij} = (\mathbf{x}_i + \mathbf{x}_j)/2$ and solve the one dimensional Riemann-problem with a Harten-Lax-van-Leer (HLL) Riemann-solver with an approximate reconstruction of the contact wave (HLLC) following Toro et al. (1994). The time integration scheme that we adopt follows the description of Springel (2010) with a common CFL-criterion for the timestep. In strong shocks driven by supernova blast waves particles can move very fast and interact with other particles, which might be on much longer time steps and cannot react accurately. To avoid this we activate all nearby particles (within a kernel radius) and put them on the same short time step. The procedure is similar to the methods described in Saitoh & Makino (2009) and Durier & Dalla Vecchia (2012).

2.2 Thermal conduction

Some of our simulations employ a prescription for thermal conduction. We follow the implementation of Jubelgas et al. (2004) with updates for this scheme presented by Petkova & Springel (2009). We implement isotropic conduction given as a local transport process for the internal energy of a fluid tracer with the heat flux \mathbf{j} .

$$\mathbf{j} = -\kappa \nabla T, \quad (1)$$

where κ is the conduction coefficient and T is the temperature. The total change of energy is

$$\rho \frac{du}{dt} = -\nabla \cdot \mathbf{j}, \quad (2)$$

with the thermal energy u and the density of the fluid ρ . The conduction equation can be obtained by inserting equation 1 into 2:

$$\frac{du}{dt} = \frac{1}{\rho} \nabla \cdot (\kappa \nabla T). \quad (3)$$

However, we note that in astrophysical plasmas the conductivity is not constant but shows a dependence on the temperature. In the Spitzer limit this is given by

$$\kappa_{\text{sp}} = 1.31 n_e \lambda_e k_B \left(\frac{k_B T_e}{m_e} \right)^{1/2}, \quad (4)$$

with the electron density n_e , its temperature T_e and its mass m_e . However, $n_e \lambda_e$ is only a function of the temperature T_e and the Coulomb-logarithm following

$$n_e \lambda_e = \frac{3^{3/2} (k_B T_e)^2}{4\pi^{1/2} e^4 \ln \Lambda}. \quad (5)$$

In the case of a constant value for the Coulomb-logarithm the Spitzer conductivity remains strongly temperature dependent

$$\kappa_{\text{sp}} = 8.2 \cdot 10^{20} \left(\frac{k_B T}{10 \text{keV}} \right)^{5/2} \frac{\text{erg}}{\text{cm s keV}}. \quad (6)$$

However, the behaviour changes for very low plasma densities where the scale length of the temperature gradient is of order the electron mean free path or even smaller. In this regime the heat flux saturates and no longer increases even if the temperature gradient rises. The saturation flux is given by

$$j_{\text{sat}} \approx 0.4 n_e k_B T \left(\frac{2k_B T}{\pi m_e} \right)^{1/2}. \quad (7)$$

In this case κ is modified to an effective κ_{eff} to smoothly change between the Spitzer and the saturated regime in the following manner

$$\kappa_{\text{eff}} = \frac{\kappa_{\text{sp}}}{1 + 4.2 \lambda_e / l_T}, \quad (8)$$

where l_T is the length scale of the temperature gradient given as $T/|\nabla T|$. While the saturation limit is mostly relevant on galaxy-cluster scales and not in the ISM, we carried out some test simulations without the heat flux limit and even without a temperature dependence of κ itself. For isolated events we do not find large differences and it seems to be more important to have a heat diffusion term in the first place. The reason for that is, that we cannot resolve the process of thermal conduction within the bubble or the shell respectively. However, what we can resolve is the interface between bubble and shell. Therefore, even a constant value for κ leads to similar results (as long as it is physically motivated), as κ at the interface of bubble and shell stays (roughly) constant.

2.3 Chemistry model

We adopt a non-equilibrium chemical model following the implementation of the 'SILCC' project (Walch et al. 2015; Girichidis et al. 2016; Gatto et al. 2017; Peters et al. 2017). This chemical model is based on Nelson & Langer (1997), Glover & Mac Low (2007a), Glover & Mac Low (2007b) and Glover & Clark (2012). We track six individual species, H_2 , H^+ , CO , H , C^+ and O as well as free electrons and assume that silicon is present in the simulation as Si^+ . Carbon is present either in single ionised form as C^+ or CO . Oxygen is present as O . H_2 and H^+ undergo several reactions, which are summarised in table 1 of Micic et al. (2012). The formation of H_2 is a dust catalysed reaction in which a dust grain captures two hydrogen atoms and the reaction becomes possible on dust surfaces. Most important for the destruction of H_2 is photo-dissociation due to the inter-stellar radiation field (ISRF), ionisation due to cosmic rays and via collisional dissociation (collisions with other species). The main channels for the formation of H^+ are collisional excitation with cosmic rays and free electrons. The destruction of H^+ is driven by recombination processes with free electrons. In the case of thermal conduction we directly assume the amount of free electrons that is predicted from solving the non-equilibrium rate equations to perform our computation of heat transfer.

2.4 Cooling and heating processes

The non-equilibrium cooling rates take into account the local density, temperature and the local chemical abundances. There are six major non-equilibrium cooling processes that are relevant for our studies, fine structure line cooling of atoms and ions (C^+ , Si^+ , O), vibration and rotation line cooling of molecules (H_2 , CO), Lyman-alpha cooling of hydrogen, collisional dissociation of H_2 , collisional ionisation of hydrogen and recombination of H^+ (both in gas phase and condensed on dust grains). The main sources for heating are given by photo-electric heating from dust grains and polycyclic aromatic hydrocarbonates (PAHs), cosmic ray ionisation, photo-dissociation of H_2 , UV-pumping of H_2 and formation of H_2 . For high temperatures ($T > 3 \cdot 10^4$ K) we adopt the cooling function by [Wiersma et al. \(2009\)](#). It assumes that the ISM is in equilibrium where the cooling due to collisional ionisation is balanced by the heating of the cosmic UV-radiation ([Haardt & Madau 2001](#)). Further, the absolute cooling rate is determined by following the model of [Aumer & White \(2013\)](#) and depends on the local gas density, gas temperature and includes metal line cooling from 11 species (H, He, C, N, O, Ne, Mg, Si, S, Ca and Fe).

2.5 Shielding mechanisms from the interstellar radiation field

For the hydrogen chemistry the ISRF photo dissociation rate R_{pd,H_2} acting on H_2 is affected by the shielding of dust and the self shielding of H_2 . Dust has the ability to absorb photons of the ISRF field and re-emit in the infrared while absorbing the energy difference. Self-shielding by molecular hydrogen is more complicated. The process normally refers to a mechanism where the photo excitation transitions become optically thick and shield each other if UV radiation is coming from a single direction. However, in the optical thick limit (high column densities) this process is prevented by the line broadening of the Lyman and Werner bands (e.g. [Gnedin & Draine 2014](#)). In this regime the self shielding by dust becomes the more important process. We include both processes, the self-shielding by dust and molecular hydrogen. This is implemented with the TREECOL-algorithm ([Clark et al. 2012; Hu et al. 2016](#)).

2.6 Numerical resolution and performance

Although the single particles have very small masses ranging from $0.1 M_\odot$ to $100 M_\odot$ this is not the effective resolution of the simulations. For methods that follow an SPH-like volume distribution the relevant spatial resolution is the size of the kernel or to be more specific the radius of compact support. For the SPH runs we use a Wendland C4 kernel with 100 neighbours while we use a cubic spline with 32 neighbours for the MFM runs to capture the fluid properties. The effective spatial and mass resolution is higher for the runs with MFM as the radius of compact support is smaller for the cubic spline and it can operate with a smaller number of neighbours. The resulting mass resolution can be calculated via

$$m_{\text{resolved}} = N_{\text{ngb}} m_{\text{gas}} \left(\frac{h}{H}\right)^3, \quad (9)$$

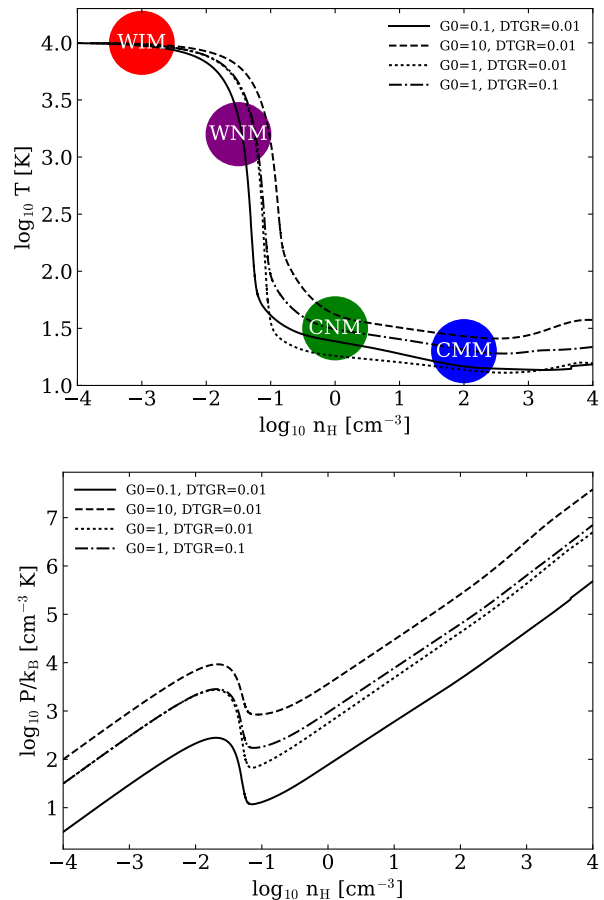


Figure 1. Equilibrium phase diagrams for temperature (top) and pressure (bottom) for a metallicity of $0.1 Z_\odot$. We show the curves for different values of G_0 and dust-to-gas ratios (DTGR). These variations only affect the high density and low temperature regimes. The four different ISM regimes, warm ionised medium (WIM), warm neutral medium (WNM), cold neutral medium (CNM) and cold molecular medium (CMM) for the SN blast wave simulations are indicated by the coloured circles. The thermally unstable regime at densities 10^{-2} to 10^{-1} cm^{-3} can be identified in the bottom panel.

where h is the smoothing length and H is the radius of compact support of the respective kernel. For the cubic spline we find the relation $h = 0.55H$ and for the Wendland C4 kernel $h = 0.45H$. Therefore, the resolution for MFM is better by about a factor of 2. While the MFM method requires more memory than SPH methods (a factor of 1.5) it is overall faster in solving the equations of hydrodynamics compared to our state-of-the-art SPH solver (for the same number of neighbours).

2.7 Initialisation and naming convention

In our default runs we adopt a metallicity of $Z = 0.1 Z_\odot$ with a constant the dust to gas ratio mass ratio of 0.01. The constant UV-background ([Haardt & Madau 2012](#)) has a normalisation factor of $G_0 = 1.7$ for the interstellar radiation field, which corresponds to the value of the solar neighbourhood. Further, we assume a cosmic ray ionisation rate of hydrogen given by $\zeta = 3 \cdot 10^{-17} \text{ s}^{-1}$. For resolution we

Table 1. Simulation parameters for supernovae in homogeneous ambient media

Simulation Name	ambient n [cm ⁻³]	ambient T [K]	metallicity [Z _⊙]	chemistry	m _{gas} [M _⊙]	solver	SN-feedback resolved
Cold Molecular Medium							
CMM-L1	100	10	0.1	100% H ₂	100	MFMH	✗
CMM-L2	100	10	0.1	100% H ₂	10	MFM	•
CMM-L3	100	10	0.1	100% H ₂	1	MFM	✓
CMM-L4	100	10	0.1	100% H ₂	0.1	MFM, SPH	✓
CMM-cond-L4	100	10	0.1	100% H ₂	0.1	SPH	✓
CMM-Z1-L1	100	10	1	100% H ₂	100	MFM	✗
CMM-Z1-L2	100	10	1	100% H ₂	10	MFM	•
CMM-Z1-L3	100	10	1	100% H ₂	1	MFM	✓
CMM-Z1-L4	100	10	1	100% H ₂	0.1	MFM	✓
CMM-Z001-L1	100	10	0.01	100% H ₂	100	MFM	✗
CMM-Z001-L2	100	10	0.01	100% H ₂	10	MFM	•
CMM-Z001-L3	100	10	0.01	100% H ₂	1	MFM	✓
CMM-Z001-L4	100	10	0.01	100% H ₂	0.1	MFM	✓
Cold Neutral Medium							
CNM-n10-L1	10	100	0.1	100% H	100	MFM	✗
CNM-n10-L2	10	100	0.1	100% H	10	MFM	•
CNM-n10-L3	10	100	0.1	100% H	1.0	MFM	✓
CNM-n10-L4	10	100	0.1	100% H	0.1	MFM, SPH	✓
CNM-n10-cond-L4	10	100	0.1	100% H	0.1	SPH	✓
CNM-L1	1	100	0.1	100% H	100	MFM, SPH	✗
CNM-L2	1	100	0.1	100% H	10	MFM, SPH	•
CNM-L3	1	100	0.1	100% H	1.0	MFM, SPH	✓
CNM-L4	1	100	0.1	100% H	0.1	MFM, SPH	✓
CNM-cond-L4	1	100	0.1	100% H	0.1	SPH	✓
CNM-Z1-L1	1	100	1	100% H	100	MFM, SPH	✗
CNM-Z1-L2	1	100	1	100% H	10	MFM, SPH	•
CNM-Z1-L3	1	100	1	100% H	1.0	MFM, SPH	✓
CNM-Z1-L4	1	100	1	100% H	0.1	MFM, SPH	✓
CNM-Z001-L1	1	100	0.01	100% H	100	MFM, SPH	✗
CNM-Z001-L2	1	100	0.01	100% H	10	MFM, SPH	•
CNM-Z001-L3	1	100	0.01	100% H	1.0	MFM, SPH	✓
CNM-Z001-L4	1	100	0.01	100% H	0.1	MFM, SPH	✓
Warm Neutral Medium							
WNM-L1	0.1	4000	0.1	100% H	100	MFM	✗
WNM-L2	0.1	4000	0.1	100% H	10	MFM	✓
WNM-L3	0.1	4000	0.1	100% H	1.0	MFM	✓
WNM-L4	0.1	4000	0.1	100% H	0.1	MFM, SPH	✓
WNM-cond-L4	0.1	4000	0.1	100% H	0.1	SPH	✓
WNM-Z1-L1	0.1	4000	1	100% H	100	MFM, SPH	✗
WNM-Z1-L2	0.1	4000	1	100% H	10	MFM	✓
WNM-Z1-L3	0.1	4000	1	100% H	1.0	MFM	✓
WNM-Z1-L4	0.1	4000	1	100% H	0.1	MFM	✓
WNM-Z001-L1	0.1	4000	0.01	100% H	100	MFM	✗
WNM-Z001-L2	0.1	4000	0.01	100% H	10	MFM	✓
WNM-Z001-L3	0.1	4000	0.01	100% H	1.0	MFM	✓
WNM-Z001-L4	0.1	4000	0.01	100% H	0.1	MFM, SPH	✓
Warm Ionised Medium							
WIM-L1	0.01	8000	0.1	100% H ⁺	100	MFM	✗
WIM-L2	0.01	8000	0.1	100% H ⁺	10	MFM	✓
WIM-L3	0.01	8000	0.1	100% H ⁺	1.0	MFM	✓
WIM-L4	0.01	8000	0.1	100% H ⁺	0.1	MFM, SPH	✓
WIM-cond-L4	0.01	8000	0.1	100% H ⁺	0.1	SPH	✓

Simulation Name	ambient n [cm ⁻³]	ambient T [K]	metallicity [Z _⊙]	chemistry	m _{gas} [M _⊙]	solver	SN-feedback resolved
Warm Ionised Medium (continued)							
WIM-Z1-L1	0.01	8000	1	100% H ⁺	100	MFM	✗
WIM-Z1-L2	0.01	8000	1	100% H ⁺	010	MFM	✓
WIM-Z1-L3	0.01	8000	1	100% H ⁺	1.0	MFM	✓
WIM-Z1-L4	0.01	8000	1	100% H ⁺	0.1	MFM	✓
WIM-Z001-L1	0.01	8000	0.01	100% H ⁺	100	MFM	✗
WIM-Z001-L2	0.01	8000	0.01	100% H ⁺	10	MFM	✓
WIM-Z001-L3	0.01	8000	0.01	100% H ⁺	1.0	MFM	✓
WIM-Z001-L4	0.01	8000	0.01	100% H ⁺	0.1	MFM	✓
WIM-n0001-L1	0.001	10000	0.1	100% H ⁺	100	MFM, SPH	✗
WIM-n0001-L2	0.001	10000	0.1	100% H ⁺	10	MFM	✓
WIM-n0001-L3	0.001	10000	0.1	100% H ⁺	1.0	MFM	✓
WIM-n0001-L4	0.001	10000	0.1	100% H ⁺	0.1	MFM	✓
WIM-n0001-cond-L4	0.001	10000	0.1	100% H ⁺	0.1	SPH	✓
WIM-Z1-L4	0.001	10000	1	100% H ⁺	0.1	MFM, SPH	✓
WIM-Z001-L4	0.001	10000	0.01	100% H ⁺	0.1	MFM, SPH	✓

refer to the gas particle mass. The four resolution levels are 100 M_⊙ (L1), 10 M_⊙ (L2), 1 M_⊙ (L3) and 0.1 M_⊙ (L4). The SN blast waves are simulated in the cold molecular medium (CMM) with $n = 100 \text{ cm}^{-3}$, the cold neutral medium (CNM) with $n = 1 \text{ cm}^{-3}$, the warm neutral medium (WNM) with $n = 0.1 \text{ cm}^{-3}$ and the warm ionised medium. Some runs have lower $Z = 0.01 Z_{\odot}$ (Z-001) and higher $Z = 1Z_{\odot}$ (Z-1) metallicities. A different number density compared to our defaults is indicated with n and the number density in units of cm^{-3} . Runs with isotropic thermal conduction are indicated by *cond*.

3 INDIVIDUAL SUPERNOVA BLAST WAVES

We present a set of simulations of individual SN blast waves in six different environments at equilibrium conditions of the ISM for our cooling model. In the upper panel of Figure 1 we show the temperature as a function of hydrogen number density for different values for a (constant) interstellar radiation field and the dust to gas ratio (DTGR). The coloured circles indicate the ISM conditions for WIM, WNM, CNM and CMM. The CMM represents regimes in dense molecular clouds ($n_H = 100 \text{ cm}^{-3}$, $T = 10 \text{ K}$, fully molecular). The CNM has higher temperatures and densities such that hydrogen is present in neutral atomic form ($n_H = 1 \text{ cm}^{-3}$, $T = 100 \text{ K}$, fully neutral). The WNM is warmer but still neutral ($n_H = 0.1 \text{ cm}^{-3}$, $T = 8000 \text{ K}$, fully neutral) and the WIM is fully ionised with long cooling times ($n_H = 0.001 \text{ cm}^{-3}$, $T = 10000 \text{ K}$, fully ionised). The pressure vs. density plot in the bottom panel highlights the pressure-unstable regime between 10^{-2} and 10^{-1} cm^{-3} . We initialise each supernova event by a kernel-weighted injection of 10^{51} erg thermal energy into all kernel particles. The initial phase of free expansion is very short (only a few 100 yr) and not modelled here. The initial conditions are summarised in Table 1.

3.1 Blast wave evolution

In Figure 2 we show the radial profiles of the hydrogen number density (top left), the temperature (top right), the ra-

dial velocity (bottom left) and the thermal pressure (bottom right) for a blast wave in the CNM at the highest resolution of 0.1 M_⊙, which implies a spatial resolution of around 1 pc. The different colours show the system at time $t = 0.03 \text{ Myr}$ (black) during the ST-phase, at $t = 0.16 \text{ Myr}$ (red) after the formation of a dense cooling shell, and at $t = 1.0 \text{ Myr}$ (blue) when the remnant starts to merge with the ISM. In the ST-phase the maximum value of the density is around 3.5 cm^{-3} . In the case of the pure adiabatic solution we would expect a maximum density of 4 cm^{-3} under constraint of the Rankine-Hugoniot jump-conditions with an adiabatic index of 5/3 which is adopted in all our simulations. After shell formation the remnant has formed a thin, cooling dominated shell with a maximum density of roughly 20 times the initial ambient density. At the end of the simulation the amplitude within the density decreases again and the remnant starts to merge with the ambient ISM. In all three stages the temperature declines as a function of the radius. After shell-formation we can observe a bump in the temperature distribution at around 10^4 K which can be identified as the dense cooling shell of the remnant. This shell grows over time as more and more gas from the initially hot bubble starts to cool. The velocities within the ST-phases are high which can lead to a velocity dispersion of roughly 10 km s^{-1} that is observed within the ISM. At later stages the remnant slows down until it finally reaches the point where it merges with the ISM. Initially, the pressure is large (especially in the bubble) but decreases about an order of magnitude within the later evolutionary stages. To understand the details of the blast waves evolution we investigate the remnant at different mass resolutions. In Figure 3 we show the remnant in the CNM during the ST-phase for all four mass resolutions that we investigated. We note that the shock is well resolved at the highest mass resolutions for the simulations CNM-L4 and CNM-L3. While the shock is still sufficiently resolved in the adiabatic regime in CNM-L2 it is completely unresolved for CNM-L1. This is mainly due to the fact that we have a lower amount of resolution elements in the same spatial region to actually resolve the shock properly in the adiabatic regime. Therefore, to capture the shock within the ST-phase a mass resolution of 10 solar masses is

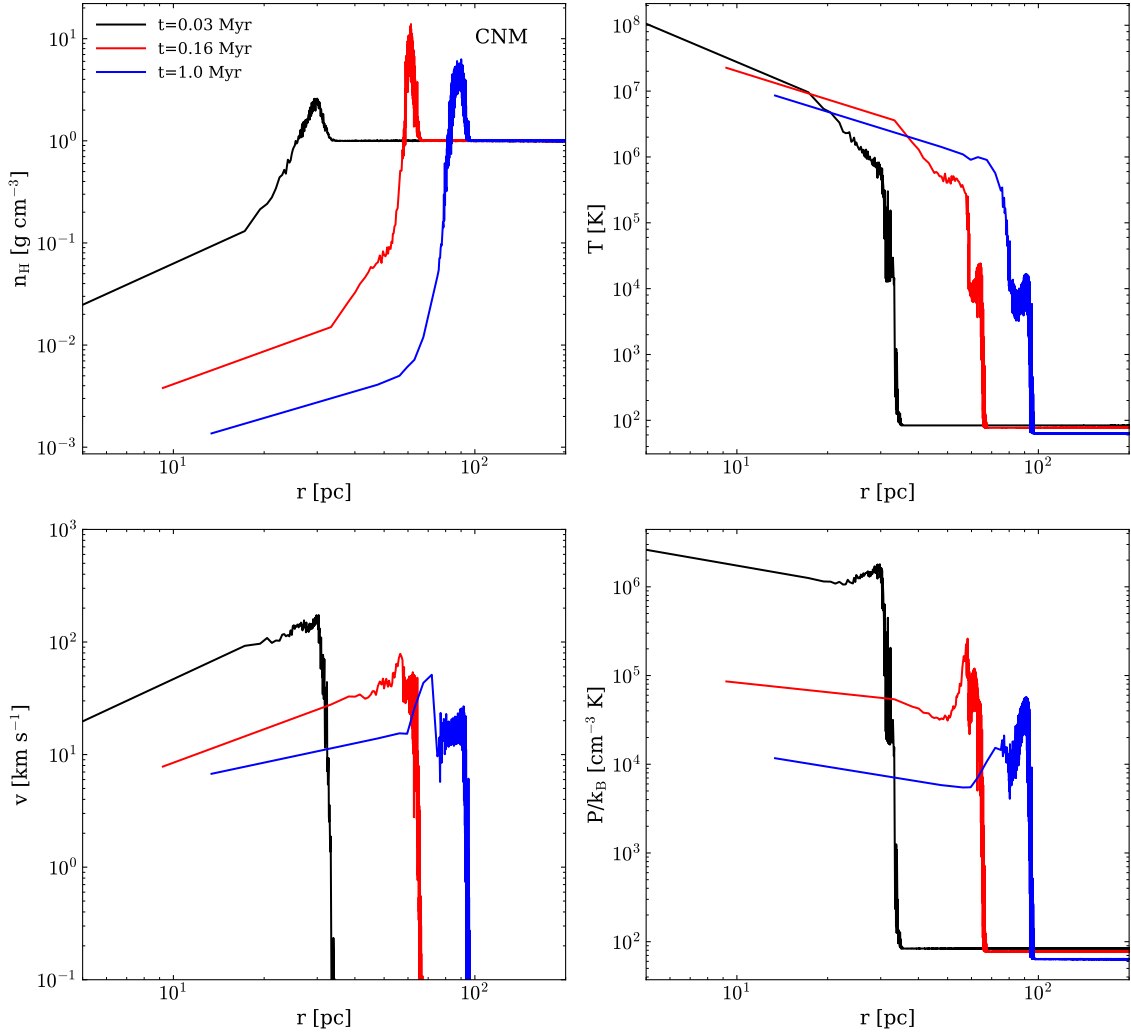


Figure 2. Hydrogen number density (top left), temperature (top right), velocity (bottom left) and pressure (bottom right) for the simulation CNM-L4 as a function of the radius. We display the results at three different points in time that represent different phases of the blast wave. The black lines indicate $t = 0.03$ Myr where the shock is in the energy conserving ST-phase. The red lines show $t = 0.14$ Myr. In this regime the cooling time is shorter than the total time of the simulation (roughly 0.08 Myr) and the system is dominated by cooling. The blue lines show the properties of the shock at the end of the simulation when the shock merges with the ambient medium. All properties of the shock are resolved in each investigated regime of the shock. *Top Left:* In the ST-phase (black line) the shock is resolved in the adiabatic regime. In the cooling dominated regime (red line) the maximum density exceeds the expected adiabatic solution by a factor 3.5. At the end of the simulation (blue line) the density decreases again and the shock starts to merge with the ambient medium. *Top Right:* The temperatures in the post-shock region are very high (above 10^8 K). When cooling dominates energy is radiated away and the temperature starts to decrease by an order of magnitude. *Bottom Left:* In the beginning the shock moves very fast outwards (a few 100 km s^{-1}) but gets slower at later times. *Bottom Right:* The pressure is roughly constant during the ST-phase of the shock but starts to decrease very fast after shell formation.

needed for the MFM-solver. We mark runs that are resolved (green check), weakly resolved (black dot) and unresolved (red crosses) in Table 1. Further, we note differences in the cooling dominated regime. At the highest mass resolutions a thin, cooling dominated shell is forming following the end of the ST-phase. The density within this supernova shell is up to 10 times higher than what we would expect to see in a pure adiabatic simulation of the shock front. However, with lower resolution this dense cooling shell becomes less and less resolved and remains unresolved at a mass resolution of $100 M_{\odot}$. We note that this becomes even worse for a different ambient configuration. If we consider the runs in the CMM

the shock is less well resolved even at higher mass resolution. In the last evolution stage of the remnant the density decreases again and starts to merge with the ambient medium for all mass resolutions. We note that in these simulations we cannot capture the phase in which the SN-remnant merges with the ambient medium as the configuration of our ambient medium is chosen to be of uniform density and zero velocity. Consequently, our ambient medium is not turbulent which would be necessary to properly capture the merging phase of the shock with the ambient medium.

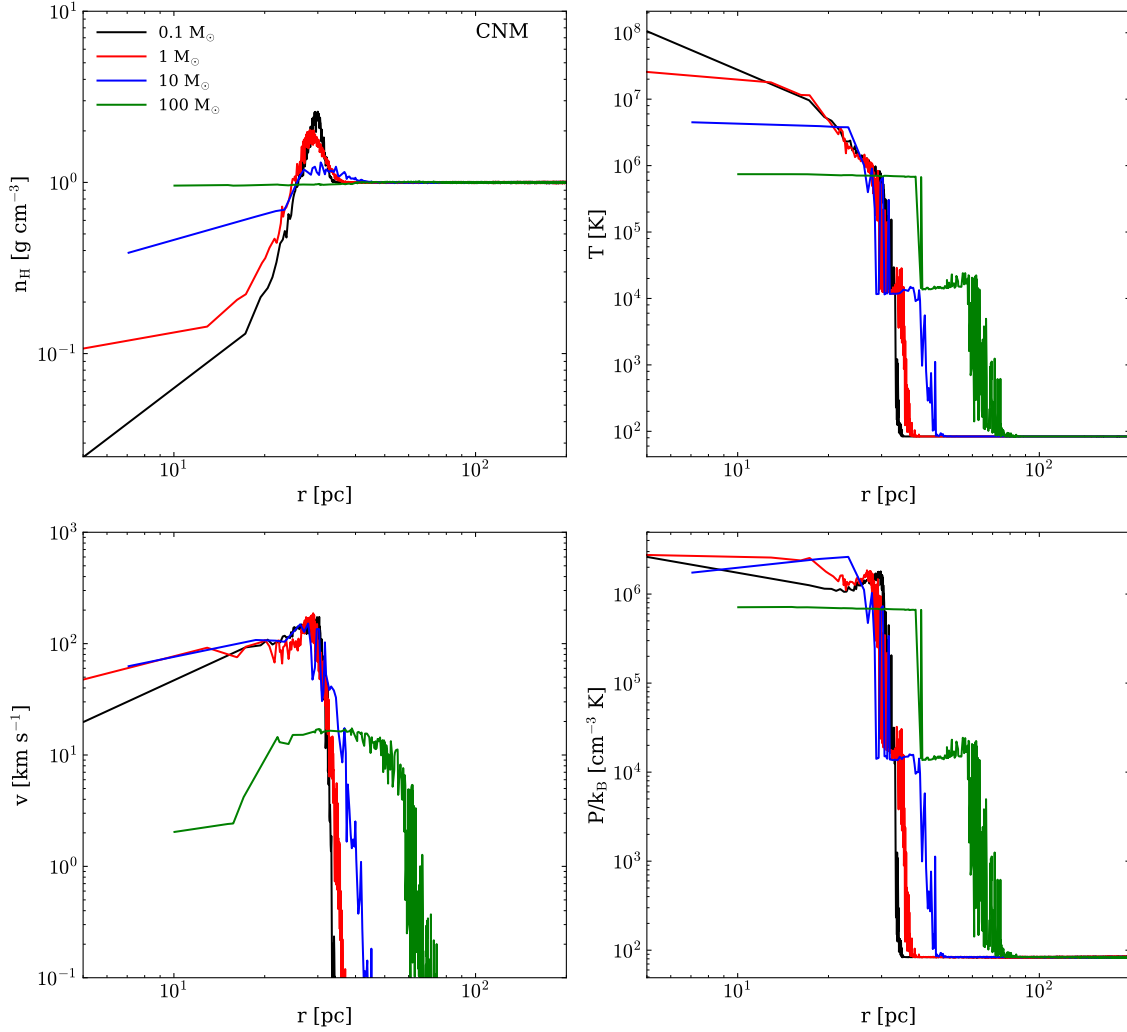


Figure 3. Different properties of the SN-remnant as a function of the radius in the ST-phase for all mass resolutions in the CNM. The black lines show the $0.1 M_{\odot}$, the red lines the $1 M_{\odot}$ resolution, the blue lines the $10 M_{\odot}$ and the green lines the $100 M_{\odot}$ resolution. *Top Left:* Density of the shock as a function of radius. With decreasing resolution the shock becomes less and less resolved. At the two highest mass resolutions we can detect the shock very well in the ST-phase. At the highest mass resolution we find the maximum density increased by a factor 3.5 compared to the ambient density. While we can still detect the shock in the ST-phase for the $10 M_{\odot}$ resolution the shock in the density completely vanishes at the lowest resolution. *Top Right:* Temperature structure of the shock. The three highest mass resolutions agree well apart from the maximum temperature within the bubble. At the lowest mass resolution, we find that the shock is at a different radial position which corresponds to the larger injection region in this regime. *Bottom Left:* Velocity structure of the shock in the ST-phase. The three highest mass resolutions agree very well, while at the lowest resolution the velocity structure remains unresolved. *Bottom Right:* Pressure in the remnant. For the three highest resolutions we find that the pressure is well resolved. For the lowest resolution the pressure in the bubble is already significantly lower, compared to the higher resolution runs.

3.2 Resolution effects

For an accurate simulation of a supernova blast wave it is important to capture the formation of the swept-up shell, which also determines the cooling properties of a supernova remnant (e.g. Kim & Ostriker 2015). For example Hu et al. (2016) have shown for SPH that the shell momentum is relatively insensitive to numerical resolution. However, the shell mass and velocity are strongly affected by higher velocities and lower shell masses at high resolution. At insufficient resolution the shell becomes too massive, slower and cools too early, resulting in a too rapid termination of the ST-phase. Similar results have been found by Kim & Ostriker (2015)

for Eulerian grid simulations. In our simulations, we define the shell as all particles with velocities $\geq 0.1 \text{ km s}^{-1}$. Further, we adopt a temperature cut. The material in the shell has a temperature below $2 \cdot 10^4 \text{ K}$. All material above this temperature cut belongs to the hot phase of the remnant. The shell radius is defined by the position of the 10 particles with the highest densities. The radial shell momentum is computed by summing up the individual particle momenta, and the shell velocity is the shell momentum divided by the shell mass.

In Figure 4 we show shell radius (top left), shell momentum (top middle), shell energy (top right), split in kinetic (blue) and thermal energy (red), shell velocity (bottom

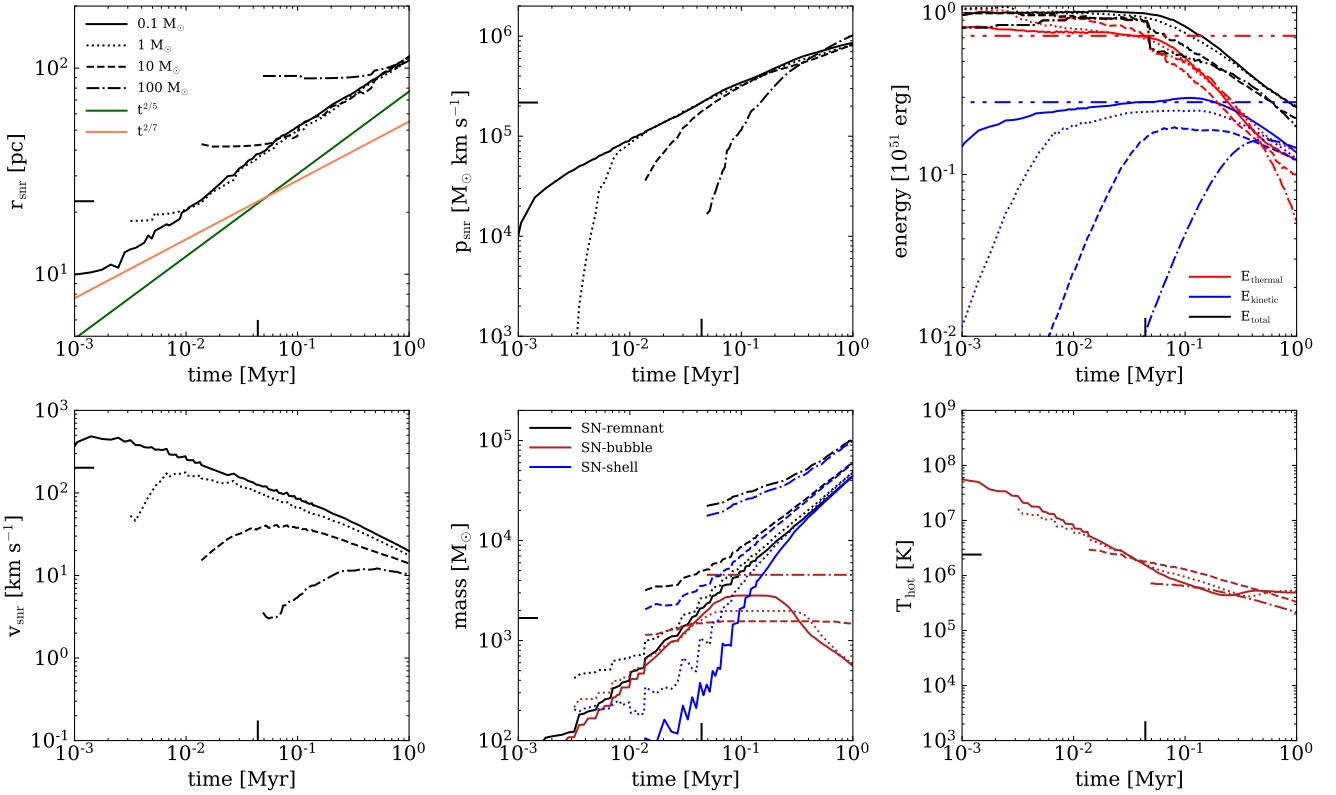


Figure 4. Evolution of supernova remnants in the CNM at four different resolution levels of $0.1 M_{\odot}$ (solid), $1 M_{\odot}$ (dotted), $10 M_{\odot}$ (dashed) and $100 M_{\odot}$ (dashed-dotted). The black markers on the axis represent the physical values at the end of the ST-phase. *Top Left:* Time evolution of the shell radius with the analytical values of $r \propto t^{2/5}$ (green) and $r \propto t^{2/7}$ (red) for Sedov phase and the momentum conserving phase, respectively. Our results converge for mass resolution higher than $10 M_{\odot}$. *Top Middle:* The shell momentum as a function of time is relatively insensitive to resolution. *Top right:* Total energy (black), kinetic energy (blue) and thermal energy (red) as a function of time. The total energy is conserved in the ST-phase with 28 per cent kinetic and 72 per cent thermal energy (dot-dot-dashed lines). The kinetic energy builds up during shell formation (we inject only thermal energy) and reaches the ST-solution only for the highest mass resolution. The $10 M_{\odot}$ run only creates ~ 20 per cent kinetic energy. *Bottom Left:* The shell velocity as a function of time strongly depends on resolution. At the end of the Sedov phase it ranges from 30 km s^{-1} to 200 km s^{-1} for low and high resolution, respectively. *Bottom Middle:* The shell mass as a function of time is smaller at higher resolution. *Bottom right:* Bubble temperature (red) as a function of time. At low mass resolution the bubble temperature and therefore its pressure remain unresolved. At mass resolution higher than $10 M_{\odot}$ the bubble temperature at the Sedov time is captured. At $100 M_{\odot}$ the temperature evolution is unresolved.

left), shell mass and bubble mass (bottom middle), as well as the bubble temperature (bottom right). We present the four resolution levels with $0.1 M_{\odot}$ (solid line), $1.0 M_{\odot}$ (dashed-line), $10 M_{\odot}$ (dash-dot-line), $100 M_{\odot}$ (dash-dot-dot-line) for a medium with $n = 1 \text{ cm}^{-3}$ consisting of neutral hydrogen (CNM-L4 to CNM-L1). The small black dashes on the axis indicate the end of the ST-phase and the numerical values of the respective quantity for this point in time. We note that instead of showing the pressure in shell and bubble, we show the temperature structure within the hot bubble. The pressure within the bubble can be computed at any time by multiplying the densities within shell and bubble with the related temperatures. In the top left panel of Figure 4 before shell formation $t < t_{\text{sf}}$ at the end of the Sedov phase, the radius is increasing as $r \propto t^{2/5}$ (Sedov 1946; Taylor 1950) (green line). At shell formation ($t_{\text{sf}} = 45000 \text{ yr}$) the slope changes $r \propto t^{2/7}$ for the momentum conserving phase. We define our Sedov-Taylor time t_{sf} as the (final) time when the thermal energy drops below the analytical value of 72 per

cent. The three highest resolution levels capture the shell radius at formation and its evolution within 10 per cent. The shell momentum (top middle panel of Figure 4) is relatively insensitive to resolution and well captured at the three highest resolution levels. Further, our results are in good agreement with results from Kim & Ostriker (2015) and Hu et al. (2016). The shell velocity and mass, however, depend strongly on resolution (bottom left and middle panel of Figure 4). With higher resolution the remnant velocity increases and the remnant mass decreases as the shock is better resolved. However, we note that a part of this trend is related to our feedback scheme. We further distinguish between the total mass of the remnant (black), the mass in the cold shell (blue) and the mass in the hot bubble (red). With decreasing resolution the mass within the bubble is lower apart from the lowest resolution run where the initially heated particles generate a too high hot mass. However, as the structure of the shell is so poorly resolved in these runs those particles cool very inefficiently and the hot mass is over predicted.

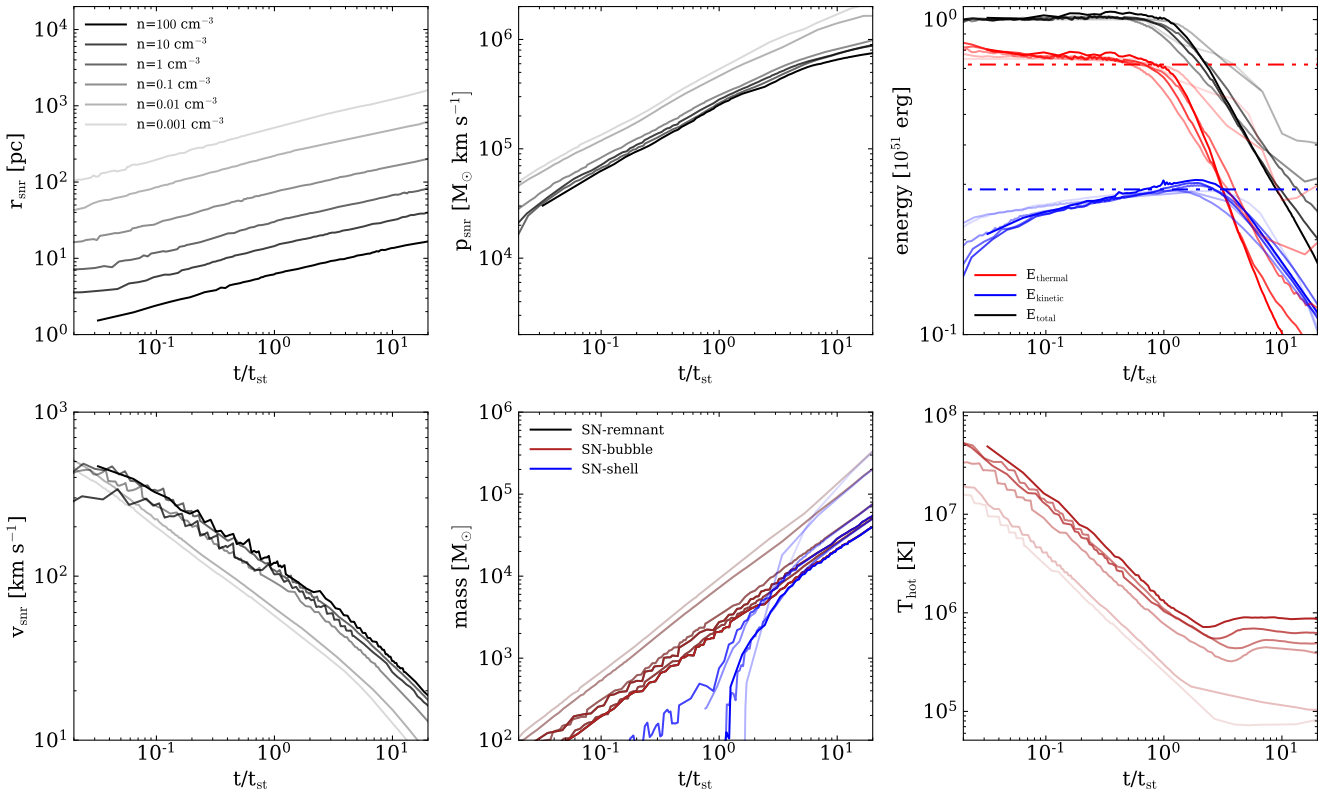


Figure 5. Comparison of physical properties of SN-blastwaves for different ambient densities for our highest all our highest resolution runs. For all runs the ST-phase is well resolved at our highest mass resolution. For better comparison we normalised the time axis to the respective ST-time that we derive in Figure 6. *Top Right:* In the high ambient media the radii become significantly smaller. While at the highest ambient medium the remnant has a size of a few parsec at the end of the ST-phase, we find that in the lowest ambient medium the remnant has a size of roughly 700 parsec at the end of the ST-phase. *Top Middle:* The remnants in ambient media with the highest density generate most momentum within the ISM. These remnants have the longest cooling times but fill the highest volume and therefore generate most momentum at the end of the ST-phase. *Top Right:* Energy in the shocked region split up in kinetic energy (blue), thermal energy (red) and total energy (black). In all environments the evolution towards the ST-phase is given and we find that 28 per cent of the energy is deposited in kinetic energy while 72 per cent is in thermal energy before cooling takes over and thermal energy is radiated away after the end of the ST-phase. *Bottom Left:* In the beginning the remnants in the lowest density environments are the fastest, while at the end of the ST-phase they are the slowest. *Bottom Middle:* The remnants with the highest mass at the end of ST-phase are those in the low density environments. Therefore, they have the highest momenta at the end of the ST-phase but also the lowest velocity. *Bottom Right:* The temperature in the bubble decreases with decreasing ambient density. This phase is important because it generates the pressure in the bubble which makes it possible to drive outflows.

For lower mass resolution we inject initially in more mass, leading to more initial swept-up material. This has consequences for the shell momentum at lower resolution. In the $10 M_{\odot}$ run the shell momentum is too high because of this reason, which renders the shell momentum a bad tracer to determine whether the ST-phase is resolved. The evolution of shell and bubble temperature is shown in the lower right panel. At the two highest resolution levels the bubble temperatures are resolved to within 10 per cent. At the lowest mass resolution the temperature structure of the hot bubble is unresolved.

3.3 Environmental dependence

The evolution of SN remnants is strongly dependent on the environment. The cooling-time scales as n^2 which has consequences for remnants in a high density environment as

well as remnants in a low density environment and leads to various different shell formation times. In Figure 6 we show the ambient densities for all our SN-remnants at the highest resolution (L4) as a function of the shell formation time t_{sf} . With increasing ambient densities the shell formation times become shorter and can last from a few 1000 years at 100 cm^{-3} to roughly 1.5 Myr at 0.001 cm^{-3} . As we simulate in three different metallicity regimes we show our best fits for the shell formation time individually for each metallicity as the dashed red line ($Z = 1Z_{\odot}$), the solid red line ($Z = 0.1Z_{\odot}$) and the dashed-dotted red line ($Z = 0.01Z_{\odot}$). For $Z = 0.1Z_{\odot}$ we additionally show the data from our six highest resolution runs to visualise the data with which we obtained the red solid line. The best fit relations as functions of the metallicity are given by:

$$t_{\text{st}}(Z = 0.01Z_{\odot}) = 5.3 \cdot 10^4 \text{ yr} \cdot n^{-0.50}, \quad (10)$$

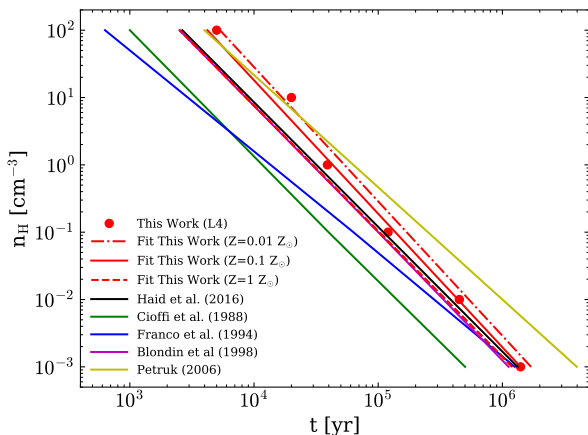


Figure 6. Shell formation times for different ambient densities at our highest resolution level. We show the data for our highest resolution run (red dots) for a metallicity of $Z = 0.1 Z_{\odot}$ (red solid line). For the two other metallicities we tested we only show the fitting function that we obtain in the $Z = 1 Z_{\odot}$ regime (red dashed line) and in the $Z = 0.01 Z_{\odot}$ regime (red dashed-dotted line). We find reasonable agreements with the fits provided by Blondin et al. (1998), Haid et al. (2016), Cioffi et al. (1988), Franco et al. (1994) and Petruk (2006). Note that all authors use slightly different cooling functions and some results are from (semi-)analytical computations.

$$t_{\text{st}}(Z = 0.1 Z_{\odot}) = 4.2 \cdot 10^4 \text{ yr} \cdot n^{-0.50}, \quad (11)$$

$$t_{\text{st}}(Z = 1 Z_{\odot}) = 2.9 \cdot 10^4 \text{ yr} \cdot n^{-0.53}. \quad (12)$$

We compare these shell formation times to previous numerical and analytical results by Blondin et al. (1998), Cioffi et al. (1988), Franco et al. (1994), Petruk (2006) and Haid et al. (2016) and find good agreement with the recent results of Haid et al. (2016) and Petruk (2006).

In Figure 5 we show the blast wave evolution for all environmental densities at the highest resolution level (L4) corresponding to $0.1 M_{\odot}$ for different properties of the individual SN-remnants for an ambient metallicity of $Z = 0.1 Z_{\odot}$. With increasing ambient number density the size of the remnants at the end of the ST-phase becomes shorter and can vary over more than an order of magnitude. The momentum at the end of the ST-phase is the largest for remnants in low density environments. For all environments apart from the highest ambient density we find a trend of an increasing kinetic energy in the PDS-phase of the remnant while the thermal energy is radiated away quickly after the end of the ST-phase. The shell velocities are the highest in the low density media where the shell and bubble masses are the highest. Further, we find that the bubble temperature is higher for higher mass densities after 10 shell formation times, while the shell temperature significantly drops due to the shorter cooling times. Finally, we note that we can resolve the ST-phase for all ambient densities at our highest mass resolution. At lower mass resolution convergence can still be obtained for the three highest mass resolutions up to an ambient density of 10 cm^{-3} . For higher ambient media a mass resolution of $1 M_{\odot}$ is required to resolve the ST-phase. We show the results for a lower density environment and our highest ambient density environment in Appendix A.

The shell formation time terminates the radial momentum generation phase (see Haid et al. 2016 for a detailed discussion of the momentum generating phases) and the remnant transits to the momentum conserving snow plough phase. In Figure 7 we show an updated version of Figure 4 of Naab & Ostriker (2017) with a comparison of the momentum gain for different ambient densities to previous estimates by Cioffi et al. (1988); Martizzi et al. (2015); Iffrig & Hennebelle (2015); Li et al. (2017); Kim & Ostriker (2015); Walch et al. (2015); Geen et al. (2016). Our results agree well in particular with Kim & Ostriker (2015) and show a momentum boost compared to the assumed initial SN momentum of $p_0 = 14181 M_{\odot} \text{ km s}^{-1}$ from a factor ~ 10 at $n = 100 \text{ cm}^{-3}$ to a factor ~ 50 at $n = 0.001 \text{ cm}^{-3}$. At low resolution this boost can be lower up to a factor of two at the highest densities. As we carried out all simulations at three different ambient metallicities, we can obtain best fit relations for all three metallicities that are given by:

$$p_{\text{st}}(Z = 0.01) = 18.0 \cdot p_0 \cdot n^{-0.16}, \quad (13)$$

$$p_{\text{st}}(Z = 0.1) = 16.4 \cdot p_0 \cdot n^{-0.18}, \quad (14)$$

$$p_{\text{st}}(Z = 1) = 12.0 \cdot p_0 \cdot n^{-0.17}. \quad (15)$$

These fitting relations are shown as the red dashed-dotted ($Z = 0.01 Z_{\odot}$), the red solid ($Z = 0.1 Z_{\odot}$) and the red dashed line ($Z = 1 Z_{\odot}$) in Figure 7. The momentum is always measured at the end of the ST-phase. We note that a remnant can still generate momentum in the pressure driven snow-plough phase until pressure equilibrium between the bubble and the shell is reached, which can lead to higher momenta by a factor of two (Haid et al. 2016; Kim & Ostriker 2015). Compared to other studies (e.g. Haid et al. 2016; Kim & Ostriker 2015) we follow the momentum gain for $Z = 0.1 Z_{\odot}$ and $Z = 0.01 Z_{\odot}$. We find a weak dependence of the final terminal momenta generated by each remnant in different metallicity environments which mostly affects the terminal momenta in the high ambient density regimes (roughly a factor of 2) while the momenta in the lowest ambient environments remain unchanged.

3.4 Chemical composition

We show the chemical evolution of SN-remnants for H_2 , H , and H^+ in the WNM, the CNM, the CNM-n10, and the CMM in Figure 8. In the WIM (top left) the initial material is fully ionised and H^+ stays the dominating chemical component of the shell even after 2 shell formation times where roughly 60 per cent of the remnant are in full ionisation. However, at ten shell formation times the remnant becomes fully neutral and also forms a tiny fraction of molecular hydrogen (below a solar mass). The CNM (top right panel) initially consists of neutral hydrogen but the whole remnant is ionised by the blast wave. Only after shell formation the remnant cools and the shell is becoming 100 per cent neutral again after 10 shell formation times. In these remnants molecular species can be ignored. For the CNM, we show a resolution study for the chemical fractions within the remnant. At the lowest mass resolution the chemical composition of the single remnant is not captured accurately. At this resolution the remnant is not fully ionised in the beginning

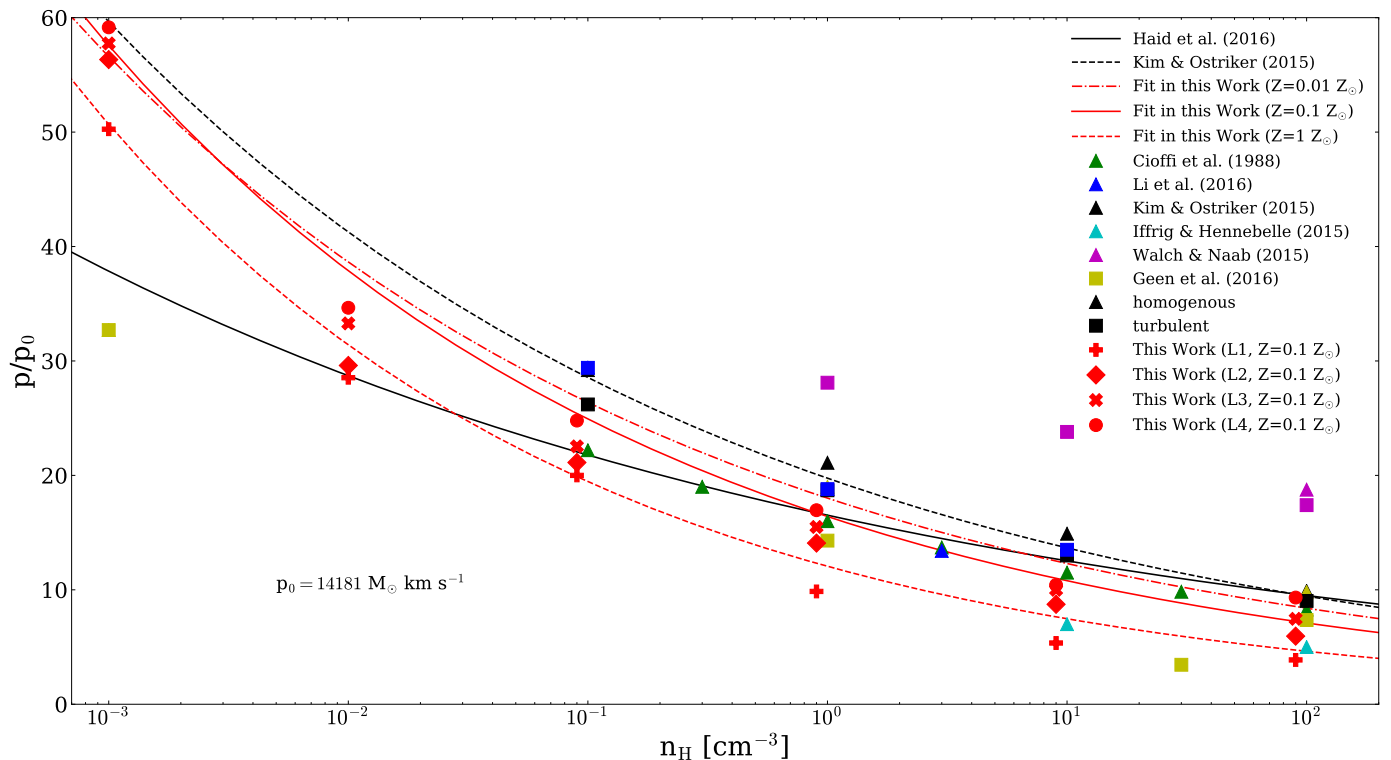


Figure 7. Momentum boost at the time of shell formation for blast waves at various environmental densities normalised to a fiducial initial momentum of $p_0 = 14181 M_\odot \text{ km s}^{-1}$. The coloured symbols show results from three dimensional numerical simulations (apart from Cioffi et al. (1988) and Haid et al. (2016)) with homogeneous (triangles), structured or turbulent (cubes) ambient media carried out with three different grid codes and a particle based SPH code. The red symbols show the supernova momenta obtained in this work at the end of the energy conserving ST-phase for our four different resolution levels in a homogeneous medium. At the lowest resolution the momenta can be underestimated by up to a factor 2. The lines show the fits from Haid et al. (2016), Kim & Ostriker (2015), and the highest resolution of this work for all three adopted metallicities. We show the results obtained for a metallicity of $0.1 Z_\odot$ as red symbols for all environmental densities and mass resolutions. We note that we shifted the red symbols slightly to the left to show the results of other work below.

and initially more mass is kept in the neutral state rather than fully ionised by the blast wave as expected. The remnant is fully neutral before shell formation. The same is true for the $10 M_\odot$ runs, although we note that here we already find a slightly dominating ionisation fraction of the remnant compared to the neutral component. For the two highest resolution runs we find that the blast wave is fully ionising the ambient medium, keeping 70 to 80 per cent of the gas ionised until shell formation. After that, cooling is dominating and the remnant starts to form neutral hydrogen and reaches the fully neutral state roughly 10 shell formation times after the appearance of the blast wave. Despite the fact that the molecular fractions are low, they also vary within at least an order of magnitude at the end of the simulation, where the low resolution remnants produce more molecular hydrogen than the high resolution ones. In higher density media (CNM-n10) we find the same behaviour (bottom left panel of Figure 8). However, we note that initially a small fraction of hydrogen of around 20 per cent is kept in the neutral phase and the formation rate of molecular hydrogen is slightly enhanced (half an order of magnitude) towards the end of the simulation. In the CMM medium (bottom left of Figure 8) we find that the some of the initially swept up mass is kept in the neutral state (again roughly 20 per cent) while the

rest is fully ionised. The formation rate of molecular hydrogen increases again and at the end of the simulation we find about half an order of magnitude lower molecular fractions than ionised rest mass of the remnant. If we continued the simulation longer the built-up of molecular hydrogen would be significant. However, we assume that remnants overlap before they reach more than 30 Sedov-times.

3.5 Comparison of different Hydro-solvers

We carried out some of our simulations employing different solvers for hydrodynamics. All simulations at our highest mass resolution are carried out with our pressure-energy SPH solver. In Figure 10 we show the comparison between the MFM-solver (solid) and the SPH-solver (dashed) for all physical quantities that we investigate. Overall, we find good agreement of the two solvers at the highest mass resolution. Most of the physical properties of the shock are captured within a few per cent. The major differences between the solvers are given in the behaviour of the thermal and kinetic energy (upper left panel of Figure 10). For the SPH-solver we find that the thermal energy is radiated away at a slightly earlier time compared to the MFM solver leading to shorter shell formation times (c.f. equation 12). Further, the SPH-

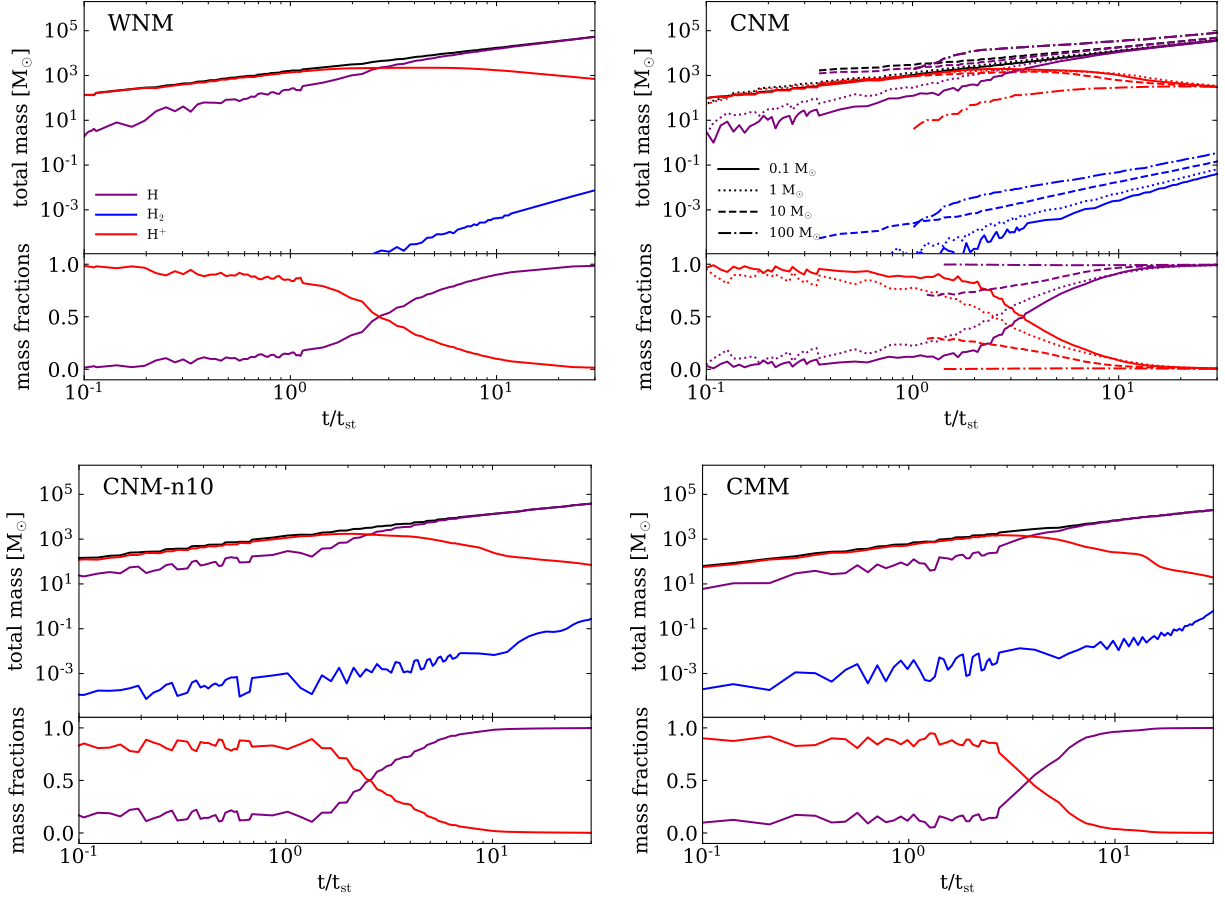


Figure 8. Chemical composition of the masses of SN-remnants in different environments of the non-equilibrium species H_2 (blue), H^+ (red) and H (purple) for the runs WNM-L4 (top right), CNM-L4 (top right), CNM-n10-L4 (bottom left) and CMM-L4 (bottom right) as a function of time. The top panels show the total mass in each species while the bottom panels show the mass fraction of each species. We observe that initially most of the molecular and neutral hydrogen is destroyed due to the heating of the injection energy. The remnants in the high density environments can preserve a small fraction of their mass in neutral hydrogen. At later times the shell becomes fully neutral again in all remnants. In all cases we can see that a little mass in molecular hydrogen builds up. However, it is below the per cent level within 10 Sedov-times. The black lines indicate the total mass in the remnant.

solver under predicts the kinetic energy within the ST-phase. The other difference that we point out is that the SPH-solver predicts a lower temperature in the hot bubble by half an order of magnitude. Therefore, the pressure within the bubble is slightly lower, which can potentially lead to less momentum generation within the PDS phase for this method. For the SPH-solvers we evaluate the results in section 5 in more detail.

4 BUILD UP OF THE HOT PHASE

Following Naab & Ostriker (2017) we can derive the expectation value for a hot phase to be established by SN-feedback. To derive the expectation value we follow a semi-analytic approach. From our simulations we can derive the radii of the remnant as a function of the environmental density. As we do not have data for different explosion energies we lack the dependence on the explosion energy compared to similar studies (e.g. Kim & Ostriker 2015). However, we tested different metallicities and can therefore carry out the semi-analytic calculations for different metallicity regimes. First,

we need to derive the dependence of the radius on the ambient density. We can fit our results for all three different regimes. Therefore, we obtain the radius of the shell at the end of the ST-phase. We find the following relations.

$$r_{\text{st}}(Z = 0.01Z_{\odot}) = 18.0 \text{ pc } n^{-0.53} \quad (16)$$

$$r_{\text{st}}(Z = 0.1Z_{\odot}) = 16.4 \text{ pc } n^{-0.52} \quad (17)$$

$$r_{\text{st}}(Z = 1Z_{\odot}) = 13.15 \text{ pc } n^{-0.52} \quad (18)$$

The expectation value for the hot phase of a SN-explosion that goes off within the hot phase of a previously occurred SNe can be written as follows

$$\epsilon_{\text{hot}} = S \frac{4\pi}{3} r_{\text{st}}^3 t_{\text{st}}, \quad (19)$$

where S is the SN-rate and r_{st} is the remnants radius at the end of the ST-phase. By substituting r_{st} with the equations 16 to 18 and t_{st} with equations 10 to 12 we find a strong power law dependence for the expectation value of the hot

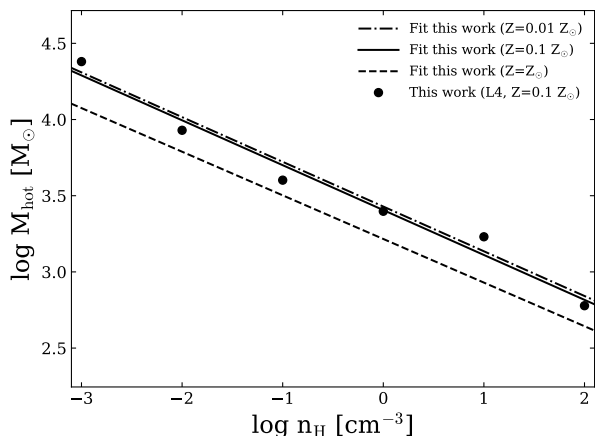


Figure 9. Peak hot mass as a function of the environmental density in which the SNe occur. We show the peak hot mass for a metallicity of $Z=0.1 Z_{\odot}$ as red dots. The red dashed, the red solid and the red dash-dotted line are the best fit relations that are obtained for the metallicities $Z=Z_{\odot}$, $Z=0.1 Z_{\odot}$ and $Z=0.01 Z_{\odot}$. We find that remnants in low density generate one order of magnitude more hot gas mass as remnants in high density environments.

phase for all three different metallicity regimes. The expectation value for the hot phase can then be determined via:

$$\epsilon_{\text{hot}}(Z = 0.01 Z_{\odot}) = S \cdot 1.310^{-6} \text{kpc}^3 \text{Myr}^{-1} n^{-2.1}, \quad (20)$$

$$\epsilon_{\text{hot}}(Z = 0.1 Z_{\odot}) = S \cdot 9.7410^{-7} \text{kpc}^3 \text{Myr}^{-1} n^{-2.1}, \quad (21)$$

$$\epsilon_{\text{hot}}(Z = 1 Z_{\odot}) = S \cdot 6.6210^{-7} \text{kpc}^3 \text{Myr}^{-1} n^{-2.1}. \quad (22)$$

Thus, we see that the expectation value for the hot phase varies only very weakly with the metallicity and we can determine it for typical values within the ISM. We assume a typical surface density of the Milky Way within the solar neighbourhood around $10 M_{\odot} \text{kpc}^{-2}$. We follow [Naab & Ostriker \(2017\)](#) and assume a Salpeter mass function and a disc height of 250 pc. From that we can determine the SN-rate S for solar neighbourhood conditions and obtain $280 \text{kpc}^{-3} \text{Myr}^{-1}$. By assuming the typical medium density within the Milky Way of $n = 1 \text{cm}^{-3}$ this gives a very low number for the expectation value for the hot phase in order of 10^{-5} to 10^{-4} . However, for SNe in lower density environments the expectation value for the hot phase becomes quickly larger and for environmental densities below 0.01 we find an expectation value greater than one due to the strong power law dependence of the expectation value with the density of the ambient medium. We note that this has consequences for the hot phase in the ISM. Once a configuration of the ISM is reached where SNe go off in low density environments our model predicts higher and higher expectation values with decreasing densities. SNe tend to go off in lower and lower density media. Cooling times for the gas increase alongside with the sizes of the remnants. Finally, this becomes a runaway process with dominating volume filling hot phase. This picture is in very good agreement with the findings from our simulations. Further, the model is in good agreement with the simulations carried out by [Girichidis et al. \(2016\)](#) who investigated the gas densities in galactic outflows and find a peak of the number density of roughly 0.01cm^{-3} . While the

remnants in the CMM have a size of a few pc, the size of remnants in the warm and hot ionised phase of the ISM can reach values up to 800 pc. Moreover, in [Figure 9](#) we show that the hot mass of the remnant significantly increases as a function of the environment. We measured the peak hot mass (maximum mass of the bubble) that is generated by SN-blastwaves in different environments and find strongly increasing masses in the hot phase in remnants below 0.1cm^{-3} . We find the following best fit relations.

$$M_{\text{hot}}(Z = 0.01 Z_{\odot}) = 2570 \cdot M_{\odot} \cdot n^{-0.29}, \quad (23)$$

$$M_{\text{hot}}(Z = 0.1 Z_{\odot}) = 2398 \cdot M_{\odot} \cdot n^{-0.29}, \quad (24)$$

$$M_{\text{hot}}(Z = 1 Z_{\odot}) = 1584 \cdot M_{\odot} \cdot n^{-0.28}, \quad (25)$$

Therefore, remnants in low density environments contribute much more to the build up of the hot phase by generating high expectation values for the hot phase alongside with high mass fractions of the hot gas. Remnants in high density media on the other hand have very low expectation values for a hot phase to form and generate only around $600 M_{\odot}$ of hot gas in the bubble which quickly cools away once the shell forms.

This has consequences for the formation of a wind driven by SNe. In this picture a wind is driven by the hot phase via the formation of a superbubble which interior is heated by SNe expanding into the bubbles of preceding SNe. Once the bubble breaks out of the disc the pressure within the bubble interior can push the shell outwards into the CGM. Hereby the outflow velocity would be limited by the sound speed within the CGM. Given a virial temperature of 10^6K for the CGM of the Milky Way this can drive outflows with a few 100km s^{-1} as they are observed (e.g. [Genzel et al. 2011](#)).

5 EFFECTS OF THERMAL CONDUCTION

Using our fiducial SPH-solver we investigate the behaviour of SN-remnants under the effect of thermal conduction. In supernova remnants, thermal conduction can influence the interface between the hot bubble and the shell by redistributing thermal energy from the bubble into the shell and mass from the shell into the bubble ([Keller et al. 2014](#); [El-Badry et al. 2019](#)). With a temperature dependent thermal conduction coefficient in the Spitzer-limit (see [Sec. 2.2](#)) we investigate differences in remnant morphology and chemistry. All our highest resolution runs have been carried out including the effect of thermal conduction. In [Figure 11](#) we show the radial profiles of the density (top left), the temperature (top left), the velocity (bottom right) and the pressure (bottom right) for the simulation CNM-Lv4. Comparing to [Figure 2](#), we find that the temperature in the run with thermal conduction is about an order of magnitude lower than in the case without thermal conduction, while the pressure remains roughly constant. The lower bubble temperatures result from heat flux from the hot bubble to the colder shell. The pressure is similar due to mass flux from the shell to the bubble. This effect has a general impact on the evolution of the remnants when thermal conduction is included.

Conduction describes a heat flux from the hot gas to the cold gas, which is counterbalanced by a mass flux from

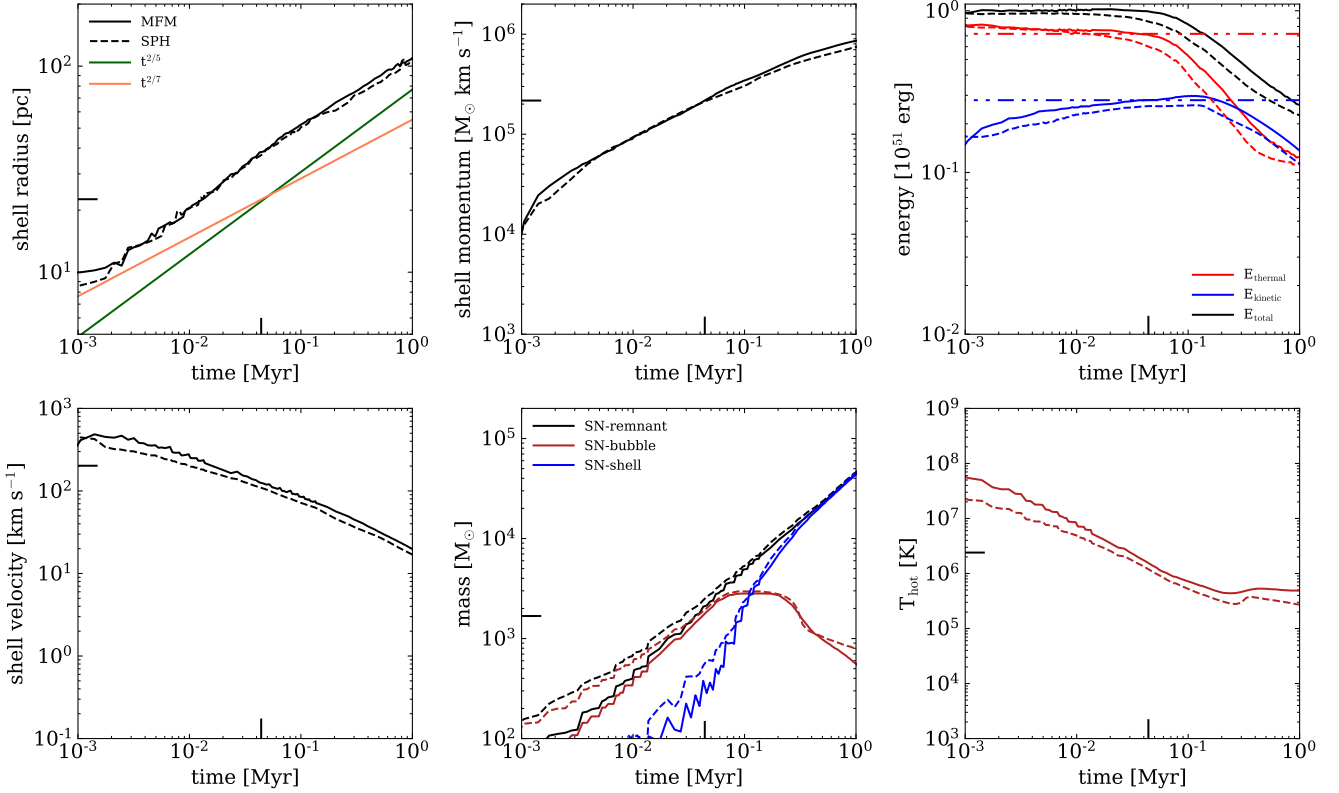


Figure 10. Comparison of the shock capturing behaviour for two different solvers, MFM (solid) and SPH (dashed). Most physical properties agree within a few percent.

the cold gas to the hot gas constrained by energy conservation. This is valid before shell formation and leads to slightly higher mass fractions of the hot gas. However, in SN-remnants cooling is active after shell formation and energy conservation is violated. Therefore, the mass flux from cold to warm gas is prohibited and the energy from the bubble that enters the shell is radiated away immediately. This can impact the general physical properties of SN-remnants. Temperature is reduced and density slightly increases. While there are quantities that are only weakly affected by thermal conduction (e.g. remnants size, velocity structure), there are others which are affected significantly. First, we note that the ST-times (times of shell formation) are shorter in the presence of thermal conduction by roughly 20 per cent. We show this in Figure 12 where we plot a comparison of the shell formation times that we find in our fiducial runs with MFM (red solid line), the SPH (red dashed line) and with SPH plus thermal heat conduction (red dashed-dotted line). Conduction leads to a redistribution of internal energy from the hot gas to the cold. This reduces temperatures and leads to a slightly enhanced cooling. Therefore, cooling times shorten and the energy conserving ST-phase terminates earlier. We find modified fitting formulas with conduction. For completeness we give the fit we obtained with SPH.

$$t_{\text{st,sph}} = 3.8 \cdot 10^4 \text{ yr} \cdot n^{-0.50}, \quad (26)$$

$$t_{\text{st,cond}} = 3.6 \cdot 10^4 \text{ yr} \cdot n^{-0.46}. \quad (27)$$

Because of the earlier termination of the ST-phase, the

momentum input with thermal conduction is lowered compared to the runs without thermal conduction. In Figure 13 we show the momentum input as a function of the environmental density and find that the SPH solver gives lower momenta by roughly 10 per cent while thermal conduction again reduces the terminal momentum by 20 per cent compared to the results that we obtain with our fiducial MFM solver. We overplot the data points from the simulation as red dots (SPH) and red crosses (SPH plus thermal conduction). The modified fitting formulas for the results with SPH and conduction yield:

$$p_{\text{st,sph}} = 14.6 \cdot p_0 \cdot n^{-0.18}, \quad (28)$$

$$p_{\text{st,cond}} = 12.9 \cdot p_0 \cdot n^{-0.18}. \quad (29)$$

However, the largest impact can be seen in the build up of the hot mass which is reduced by 40 per cent. We show the results in 14 for MFM (solid line), SPH (dashed line) and conduction (dashed-dotted line). While the results for MFM and SPH only differ in the per cent regime, the hot mass is reduced 40 per cent in the runs with thermal conduction. We note that before cooling takes over the hot mass slightly increased due to the mass flux from warm to hot gas. For thermal conduction we find the dependence of the hot mass as function of the environmental density as follows:

$$M_{\text{hot,cond}} = 1580 \cdot M_{\odot} \cdot n^{-0.29}. \quad (30)$$

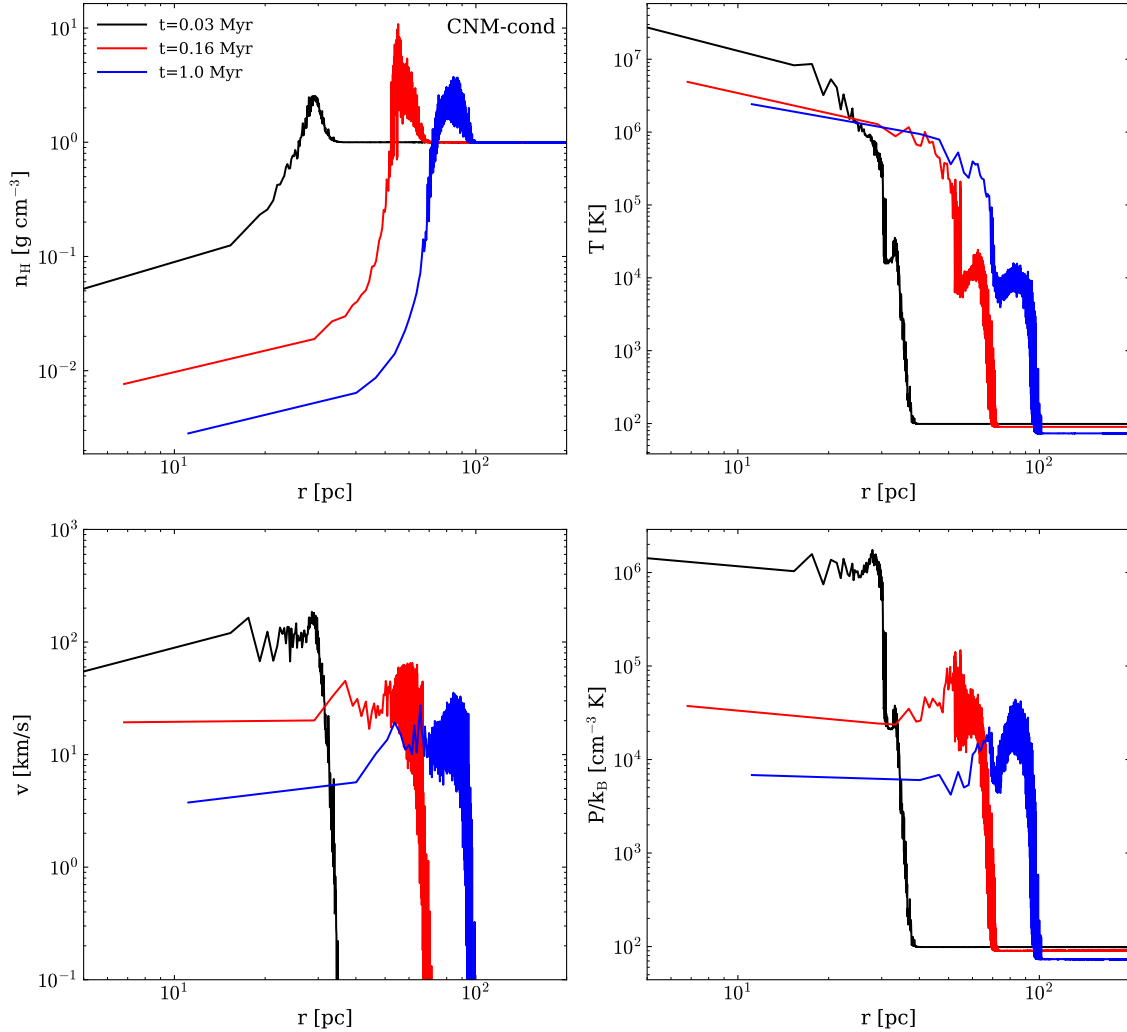


Figure 11. Same as Figure 4 but with the effect of isotropic thermal conduction. We find slightly lower temperatures in the bubble and higher densities in the shell.

Further, we find an impact of thermal conduction on the chemical composition of the SN-remnant. Overall, the effect is minor. Therefore, we show the results for the run CNM-cond in Figure 15. Initially, the majority of the gas is ionised in the case with and without conduction but with conduction the ionising fraction is lightly reduced (by roughly 5 per cent). Because cooling is slightly more efficient in the presence of conduction, the build-up of neutral hydrogen in the shell is slightly enhanced. This then leads to higher formation rates of molecular hydrogen which is increased by a factor of two.

6 CONCLUSIONS

6.1 Summary

We carried out three dimensional simulations of isolated SNe that include a non-equilibrium cooling and a chemical model that tracks the formation (and destruction) of H_2 . The canonical SN-energy of 10^{51} erg is coupled by pure thermal injection to one kernel size the centre of a box with

uniform density and tested four different mass resolutions of $0.1 M_\odot$, $1 M_\odot$, $10 M_\odot$ and $100 M_\odot$. The energy is distributed weighted by the kernel. We focus on the convergence of physical properties at the end of the ST-phase to constrain the resolution requirements for a SN-feedback scheme that can be applied in high resolution simulations of galaxy formation and evolution. Specifically, we tested the behaviour of two different, widely used numerical methods for solving Euler's equations. We tested the implications of this feedback scheme with a modified 'pressure-energy' SPH solver and the higher order meshless finite mass (MFM) solver which utilises a second order reconstruction of Euler's equations by solving the Riemann problem on the one dimensional surface between two fluid tracers to obtain the fluid fluxes. The usage of the chemical model allows us to follow the formation and destruction processes of molecular, neutral and ionised gas within isolated SN-remnants as they currently can be modelled in simulations of galaxy formation and evolution. We carried out reference runs with thermal conduction to investigate the effects of the heat flux between SN-bubble and the cold material in the remnant.

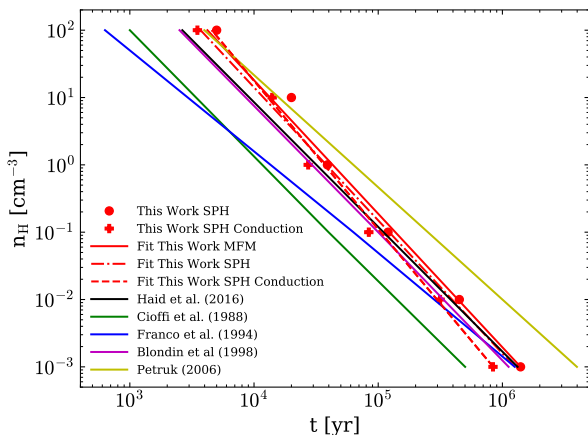


Figure 12. Same as Figure 6 for the results that we obtain with SPH (red dashed) and SPH with heat conduction (red dashed dotted). For reference we overplot the results we obtained with MFM. We find slightly shorter shell formation times for the SPH-solver than we find for the MFM solver. Moreover, thermal conduction further shortens the shell formation time.

(i) *Morphology of the shock:* We can capture three stages in the evolution of a SN-remnant. In the ST-phase we resolve the adiabatic regime defined by the Rankine-Hugoniot jump conditions with an accuracy of up to 10 per cent that is limited by the behaviour of our underlying numerical scheme. After the ST-phase the remnant enters the PDS-phase in which they can further increase momentum due to the high pressure in the bubble behind the shell. This pushes the shell further outwards until pressure equilibrium with the shell is reached and the shell moves forward with roughly constant momentum and reaches the MCS-phase. Finally, the remnant starts to merge with the ambient ISM. We can capture the shocks morphology reasonably well at our three highest resolution levels. However, at the lowest resolution level the shock remains unresolved.

(ii) *Dependence on the environment:* We carried out explosions for six different environmental densities of SN-remnants alongside the equilibrium cooling curve. For all these remnants we computed the end of the ST-phase and find a power law scaling of the termination time of the ST-phase which is within a 30 per cent agreement compared to the work of Blondin et al. (1998), Petruk (2006) and Haid et al. (2016). We investigate eight physical quantities as a function of time including radius, momentum, energy distribution, velocity structure, remnant mass, bubble-mass, shell-mass as well as the bubble temperature. At the end of the ST-phase our resolved runs agree very well with the results of studies of the same kind (e.g. Kim & Ostriker 2015; Haid et al. 2016), although we note that our default metallicity is $0.1 Z_{\odot}$ because we aim for understanding SN-feedback in low metallicity environments. Most quantities can be resolved at a resolution of $10 M_{\odot}$ in all relevant density regimes of the ISM. We specifically highlight this in the context of the momentum that has been generated during the ST-phase and the generation of the hot phase (the hot mass and the temperature evolution in the bubble). The feedback can then be resolved as a combination of those two quantities. Momentum is needed to move particles through

the ISM and generate turbulence. The hot phase is needed to generate pressure in the ISM which is necessary to launch galactic winds that can impact the CGM of a galaxy. Further, we determine a fit to the SN-momenta that are injected in different regions of the ISM based on our highest resolution remnants which can be adopted for feedback schemes in simulations of galaxy formation and evolution that do not resolve the ST-phase explicitly.

(iii) *Chemistry of single SN-remnants:* We investigate the chemical composition in the simulated SN-remnants. We note that the remnants in the low density environments contribute to the build up of the hot phase but the remnants become fully neutral after a few cooling times. They do not contribute to the formation of molecular hydrogen because the densities in the swept up mass remain low. In the CNM the mass in the swept up region is fully ionised. After cooling sets in the remnant becomes neutral after a few cooling times again. However at the end of the simulation ($t=1$ Myr) we find around one per cent of the remnant mass in neutral hydrogen. In the CMM the SN destroys most of the molecular hydrogen and leads to an ionisation of the swept up mass. We find that a small fraction (around 10 per cent) of the remnants mass remain in the neutral hydrogen phase. After cooling set in most of the material cools quickly and recombination with the free electrons leads to the formation of neutral hydrogen.

(iv) *Role of thermal conduction:* Thermal conduction leads to a decrease in temperature and to an increase in density in the shell. Thermal energy can be transported from the hot phase to the cold phase while mass from the cold phase is transported to the hot phase. Once cooling becomes relevant the mass flux towards the hot bubble is suppressed because the thermal energy that is transported from the bubble to the shell is instantly radiated away. Thermal conduction makes cooling slightly more efficient and leads to slightly less momentum generation (by 10 per cent). The quantity that is most affected by thermal conduction is the peak hot mass within the hot bubble which decreases by roughly 40 per cent compared to the runs without conduction. Due to an increase of the densities within the shell the formation rate of molecular hydrogen increases roughly by a factor of two. Moreover, we find good agreement of our results with the recent work of El-Badry et al. (2019) who investigated the effects of cooling and thermal conduction in simulations of one-dimensional super-bubbles.

6.2 Model limitations

Although we find good agreement of our results with other theoretical studies we are still limited by some assumptions we already made in section 2. For the isolated remnants we assumed that they occur in an environment with a constant ambient density. Given the highly turbulent structure of the ISM (e.g. Elmegreen & Scalo 2004) this is a rather simplified assumption. Further, we excluded the fact that massive stars normally shape their environment and ionise the surrounding ambient medium due to stellar wind prior to the core collapse event, which renders our assumption of a core collapse event in a fully molecular medium untrue. However, because in this regime we initially destroy all of the molecular hydrogen it does not influence the formation rate after shell formation. Further we neglected that each

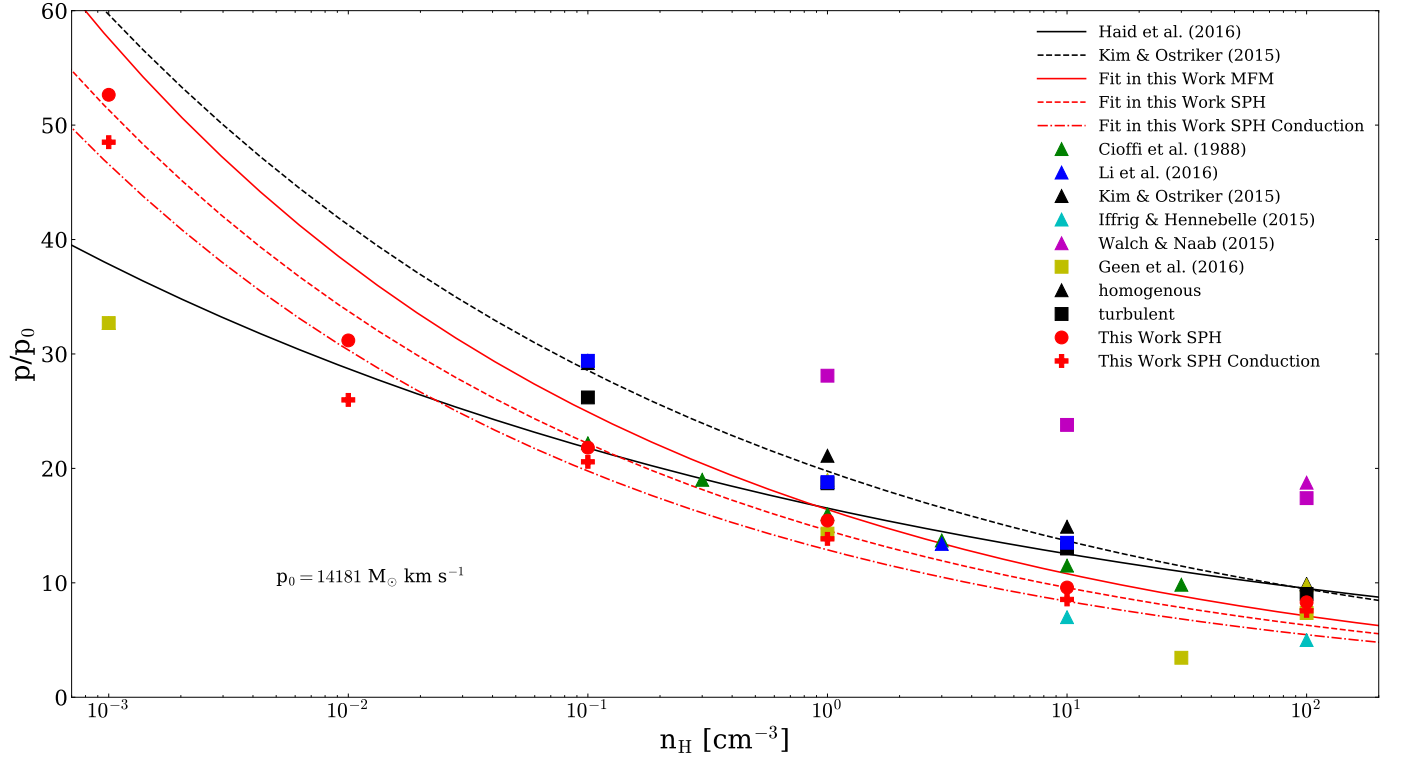


Figure 13. Same as Figure 7 for the runs with SPH (red dashed) and thermal conduction (red dashed dotted). We directly overplot the data points we obtained for SPH (red dots) and for the runs including heat conduction (red crosses). In comparison with MFM we generally find that the momentum is reduced by roughly 10 per cent for SPH and 20 per cent with SPH and heat conduction.

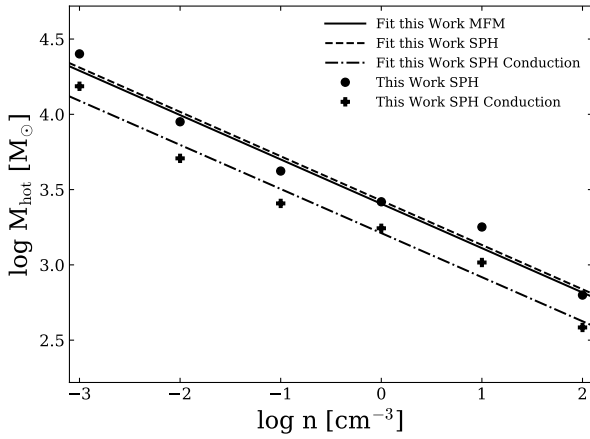


Figure 14. Same as Figure 9 for the runs that are carried out with SPH (dashed) and with SPH and conduction (dashed-dotted). While we only find weak differences between MFM and SPH in the peak hot mass we find that thermal conduction can reduce the peak hot mass by roughly 40 per cent.

remnant ejects mass in the explosion, which initially alters the chemical composition of the remnant prior to shell formation. The injection of metals and dust in the explosion would significantly shorten the cooling time and increase the formation rate of the molecules. Further, we do not consider magnetic fields in the shock. This could change the picture again because of the additional pressure component

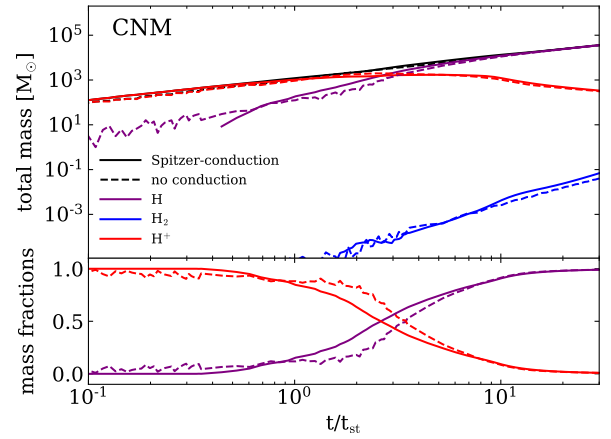


Figure 15. Comparison between the chemical evolution of the shell without the effect of thermal conduction (solid) and with thermal conduction (dashed) for the different species that the non-equilibrium model follows. We find slightly increased fractions for the H^+ in the runs that include thermal conduction in the beginning of the simulation. At later times the ionising fraction of hydrogen decreases faster than in the run without thermal heat conduction.

(the same is valid for cosmic rays). Moreover, in the case of the runs including thermal conduction it remains unclear to which degree the behaviour is driven by the numerics of the underlying scheme. Here, the crucial point is to resolve the

structure of the hot and the cold phase which we do in our two highest resolution runs. If this can be done the effect is physical, if not it remains unclear whether the results have any physical impact. Further, we note that our resolution is far too low to resolve the internal heat fluxes within the bubble or the shell (once it has formed).

ACKNOWLEDGEMENTS

UPS thanks Eirini Batziou, Andreas Burkert, Chris Byrohl, Klaus Dolag, Joseph O’Leary, Rhea Silvia Remus, Felix Schulze and Simon White for helpful discussions and insights on the physics of the interstellar medium. UPS thanks Volker Springel and Prateek Sharma for useful discussion on thermal heat conduction. UPS thanks Jeong-Gyu Kim for his comments on the ISM in equilibrium. The authors gratefully acknowledge the computing time granted by the c2pap-cluster in Garching under the project number pr27mi where most of this work has been carried out. UPS and BPM are funded by the Deutsche Forschungsgemeinschaft (DFG, German Research Foundation) with the project number MO 2979/1-1. TN acknowledges support by the DFG Cluster of Excellence ‘Origin and Structure of the Universe’ and its successor ‘Origins’. The Flatiron Institute is supported by the Simons Foundation. SWG acknowledges support by the European Research Council via ERC Starting Grant RAD-FEEDBACK (no. 679852) and by the German Science Foundation via CRC956, Project C5.

REFERENCES

- Agertz O., Kravtsov A. V., Leitner S. N., Gnedin N. Y., 2013, *ApJ*, **770**, 25
- Aumer M., White S. D. M., 2013, *MNRAS*, **428**, 1055
- Behroozi P. S., Conroy C., Wechsler R. H., 2010, *ApJ*, **717**, 379
- Behroozi P., Wechsler R., Hearin A., Conroy C., 2018, arXiv e-prints,
- Blondin J. M., Wright E. B., Borkowski K. J., Reynolds S. P., 1998, *ApJ*, **500**, 342
- Castor J., McCray R., Weaver R., 1975, *ApJ*, **200**, L107
- Cioffi D. F., McKee C. F., Bertschinger E., 1988, *ApJ*, **334**, 252
- Clark P. C., Glover S. C. O., Klessen R. S., 2012, *MNRAS*, **420**, 745
- Cohen E., Piran T., Sari R., 1998, *ApJ*, **509**, 717
- Cox D. P., 1972, *ApJ*, **178**, 159
- Cox D. P., Smith B. W., 1974, *ApJ*, **189**, L105
- Diesing R., Caprioli D., 2018, *Physical Review Letters*, **121**, 091101
- Draine B. T., 2011, *Physics of the Interstellar and Intergalactic Medium*. Princeton University Press
- Durier F., Dalla Vecchia C., 2012, *MNRAS*, **419**, 465
- Dwek E., 1998, *ApJ*, **501**, 643
- El-Badry K., Ostriker E. C., Kim C.-G., Quataert E., Weisz D. R., 2019, arXiv e-prints,
- Elmegreen B. G., Scalo J., 2004, *ARA&A*, **42**, 211
- Emerick A., Bryan G. L., Mac Low M.-M., 2019, *MNRAS*, **482**, 1304
- Falle S. A. E. G., 1975, *MNRAS*, **172**, 55
- Ferrière K., 1998, *ApJ*, **497**, 759
- Fielding D., Quataert E., Martizzi D., 2018, *MNRAS*, **481**, 3325
- Forbes J. C., Krumholz M. R., Goldbaum N. J., Dekel A., 2016, *Nature*, **535**, 523
- Franco J., Miller III W. W., Arthur S. J., Tenorio-Tagle G., Terlevich R., 1994, *ApJ*, **435**, 805
- Fransson C., Larsson J., Spyromilio J., Leibundgut B., McCray R., Jerkstrand A., 2016, *ApJ*, **821**, L5
- Frisch P. C., Redfield S., Slavin J. D., 2011, *ARA&A*, **49**, 237
- Gaburov E., Nitadori K., 2011, *MNRAS*, **414**, 129
- Gaffet B., 1983, *ApJ*, **273**, 267
- Gatto A., et al., 2015, *MNRAS*, **449**, 1057
- Gatto A., et al., 2017, *MNRAS*, **466**, 1903
- Geen S., Hennebelle P., Tremblin P., Rosdahl J., 2016, *MNRAS*, **463**, 3129
- Gentry E. S., Krumholz M. R., Dekel A., Madau P., 2017, *MNRAS*, **465**, 2471
- Genzel R., et al., 2011, *ApJ*, **733**, 101
- Girichidis P., et al., 2016, *MNRAS*, **456**, 3432
- Glover S. C. O., Clark P. C., 2012, *MNRAS*, **421**, 9
- Glover S. C. O., Mac Low M.-M., 2007a, *ApJS*, **169**, 239
- Glover S. C. O., Mac Low M.-M., 2007b, *ApJ*, **659**, 1317
- Gnedin N. Y., Draine B. T., 2014, *ApJ*, **795**, 37
- Gotthelf E. V., Koralesky B., Rudnick L., Jones T. W., Hwang U., Petre R., 2001, *ApJ*, **552**, L39
- Grefenstette B. W., et al., 2014, *Nature*, **506**, 339
- Guedes J., Callegari S., Madau P., Mayer L., 2011, *ApJ*, **742**, 76
- Gupta S., Nath B. B., Sharma P., Eichler D., 2018, *MNRAS*, **473**, 1537
- Haardt F., Madau P., 2001, in Neumann D. M., Tran J. T. V., eds, *Clusters of Galaxies and the High Redshift Universe Observed in X-rays*. p. 64 ([arXiv:astro-ph/0106018](https://arxiv.org/abs/astro-ph/0106018))
- Haardt F., Madau P., 2012, *ApJ*, **746**, 125
- Haid S., Walch S., Naab T., Seifried D., Mackey J., Gatto A., 2016, *MNRAS*, **460**, 2962
- Hopkins P. F., 2015, *MNRAS*, **450**, 53
- Hopkins P. F., et al., 2018, *MNRAS*, **480**, 800
- Hu C.-Y., Naab T., Walch S., Moster B. P., Oser L., 2014, preprint, ([arXiv:1402.1788](https://arxiv.org/abs/1402.1788))
- Hu C.-Y., Naab T., Walch S., Glover S. C. O., Clark P. C., 2016, *MNRAS*, **458**, 3528
- Hu C.-Y., Naab T., Glover S. C. O., Walch S., Clark P. C., 2017, *MNRAS*, **471**, 2151
- Iffrig O., Hennebelle P., 2015, *A&A*, **576**, A95
- Indebetouw R., et al., 2014, *ApJ*, **782**, L2
- Janka H.-T., Hanke F., Hüdepohl L., Marek A., Müller B., Obergaullinger M., 2012, *Progress of Theoretical and Experimental Physics*, **2012**, 01A309
- Jubelgas M., Springel V., Dolag K., 2004, *MNRAS*, **351**, 423
- Kamenetzky J., et al., 2013, *ApJ*, **773**, L34
- Keller B. W., Wadsley J., Benincasa S. M., Couchman H. M. P., 2014, *MNRAS*, **442**, 3013
- Kim C.-G., Ostriker E. C., 2015, *ApJ*, **802**, 99
- Kim C.-G., Ostriker E. C., Raileanu R., 2017, *ApJ*, **834**, 25
- Kobayashi C., Karakas A. I., Umeda H., 2011, *MNRAS*, **414**, 3231
- Könyves V., Kiss C., Moór A., Kiss Z. T., Tóth L. V., 2007, *A&A*, **463**, 1227
- Koo B.-C., McKee C. F., 1992, *ApJ*, **388**, 93
- Lanson N., Vila J., 2008, *SIAM J. Numer. Anal.*, **46**, 1935
- Li M., Bryan G. L., Ostriker J. P., 2017, *ApJ*, **841**, 101
- Mac Low M.-M., Klessen R. S., 2004, *Reviews of Modern Physics*, **76**, 125
- Mac Low M.-M., McCray R., 1988, *ApJ*, **324**, 776
- Marinacci F., Pakmor R., Springel V., 2014, *MNRAS*, **437**, 1750
- Martizzi D., Faucher-Giguère C.-A., Quataert E., 2015, *MNRAS*, **450**, 504
- Matsuura M., et al., 2011, *Science*, **333**, 1258
- McCray R., Kafatos M., 1987, *ApJ*, **317**, 190
- McKee C. F., Ostriker J. P., 1977, *ApJ*, **218**, 148
- Micic M., Glover S. C. O., Federrath C., Klessen R. S., 2012, *MNRAS*, **421**, 2531

- Mocz P., Vogelsberger M., Sijacki D., Pakmor R., Hernquist L., 2014, *MNRAS*, **437**, 397
- Moster B. P., Macciò A. V., Somerville R. S., Johansson P. H., Naab T., 2010, *MNRAS*, **403**, 1009
- Moster B. P., Naab T., White S. D. M., 2013, *MNRAS*, **428**, 3121
- Moster B. P., Naab T., White S. D. M., 2018, *MNRAS*, **477**, 1822
- Naab T., Ostriker J. P., 2017, *ARA&A*, **55**, 59
- Nelson R. P., Langer W. D., 1997, *ApJ*, **482**, 796
- Ohlin L., Renaud F., Agertz O., 2019, arXiv e-prints,
- Ostriker J. P., McKee C. F., 1988, *Reviews of Modern Physics*, **60**, 1
- Peters T., et al., 2017, *MNRAS*, **466**, 3293
- Petkova M., Springel V., 2009, *MNRAS*, **396**, 1383
- Petruk O., 2006, arXiv Astrophysics e-prints,
- Saitoh T. R., Makino J., 2009, *ApJ*, **697**, L99
- Scalo J., Elmegreen B. G., 2004, *ARA&A*, **42**, 275
- Sedov L. I., 1946, Dokl. Akad. Nauk SSSR, **52**, 17
- Sedov L. I., 1959, Similarity and Dimensional Methods in Mechanics
- Seifried D., Walch S., Haid S., Girichidis P., Naab T., 2018, *ApJ*, **855**, 81
- Somerville R. S., Davé R., 2015, *ARA&A*, **53**, 51
- Springel V., 2005, *MNRAS*, **364**, 1105
- Springel V., 2010, *MNRAS*, **401**, 791
- Spyromilio J., Meikle W. P. S., Learner R. C. M., Allen D. A., 1988, *Nature*, **334**, 327
- Taylor G., 1950, *Proceedings of the Royal Society of London Series A*, **201**, 159
- Thornton K., Gaudlitz M., Janka H.-T., Steinmetz M., 1998, *ApJ*, **500**, 95
- Tomisaka K., Ikeuchi S., 1986, *PASJ*, **38**, 697
- Toro E. F., Spruce M., Speares W., 1994, *Shock Waves*, **4**, 25
- Walch S., et al., 2015, *MNRAS*, **454**, 238
- Wang L., Dutton A. A., Stinson G. S., Macciò A. V., Penzo C., Kang X., Keller B. W., Wadsley J., 2015, *MNRAS*, **454**, 83
- Weaver R., McCray R., Castor J., Shapiro P., Moore R., 1977, *ApJ*, **218**, 377
- Wiersma R. P. C., Schaye J., Smith B. D., 2009, *MNRAS*, **393**, 99
- Woltjer L., 1972, *ARA&A*, **10**, 129

APPENDIX A: DIFFERENT REGIONS OF THE ISM

In this section we show the results for the runs CMM (Figure A1) and WNM (Figure A2) with the MFM-solver to investigate the solvers behaviour in capturing the ST-phase as a function of environment. For the higher density environment it is much more difficult to resolve the ST-phase at low mass resolution. While most properties are still within 50 per cent in comparison to Kim & Ostriker (2015) the hot phase remains less and less resolved at low mass resolution. The terminal momentum is still well resolved even at lower resolution. However, as we pointed out in section 3.2 this is a result of the feedback scheme where the thermal energy is injected into the 32 nearest neighbours which leads to an overestimate of the shell momentum that scales with the particle mass. Therefore, the terminal momentum remains a weak measure to determine whether the ST-phase is resolved or not. Even, if 'correct' terminal momentum is injected and particles move through the volume the feedback remains ineffective as long as the temperatures in shell and bubble are unresolved which then generate the pressure in the ISM. For the low density environments all important

physical quantities can be properly captured with a mass resolution of $10 M_{\odot}$. The crucial point in this regime is the long cooling times which are longer than 0.1 Myr. Because of this long cooling time and the negligible cooling losses the hot phase in the bubble has time to build up and can be resolved even at lower mass resolutions. As already pointed out above the momentum seems to be converged between all mass resolutions in this environment which is again due to the fact that we sweep up too much mass with our feedback scheme within the ST-phase which counterbalances the poorly resolved velocity structure of the shell which leads to the correct momentum even at lowest mass resolution. However, because in this regime we also revolve the temperature structure of the shell and the bubble the feedback remains resolved because it generates enough pressure within the ISM.

This paper has been typeset from a $\text{\TeX}/\text{\LaTeX}$ file prepared by the author.

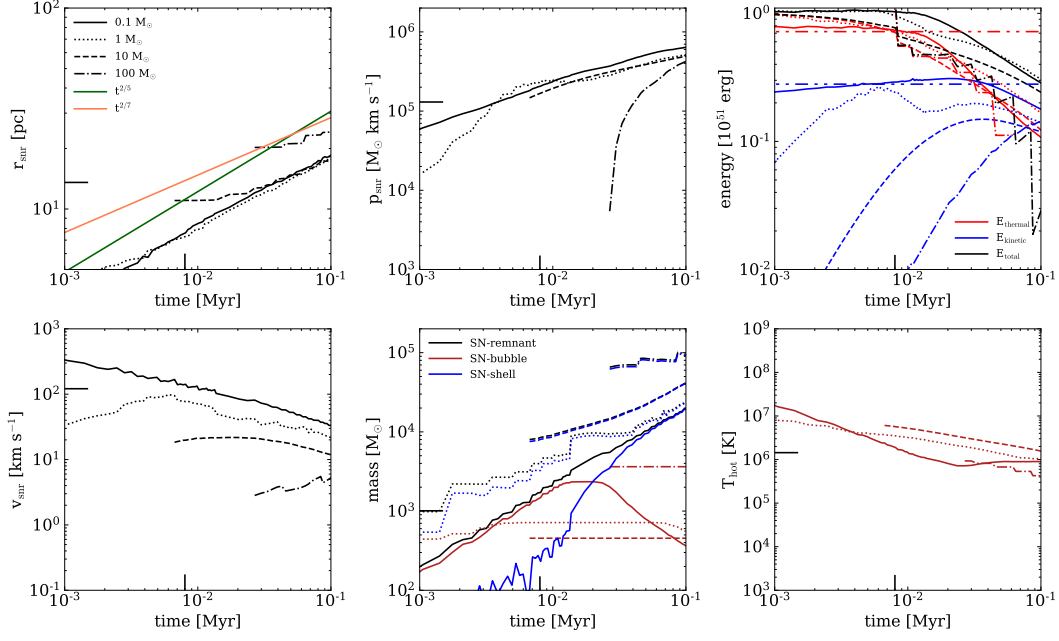


Figure A1. Same as Figure 4 for an ambient density of 100 cm^{-3}

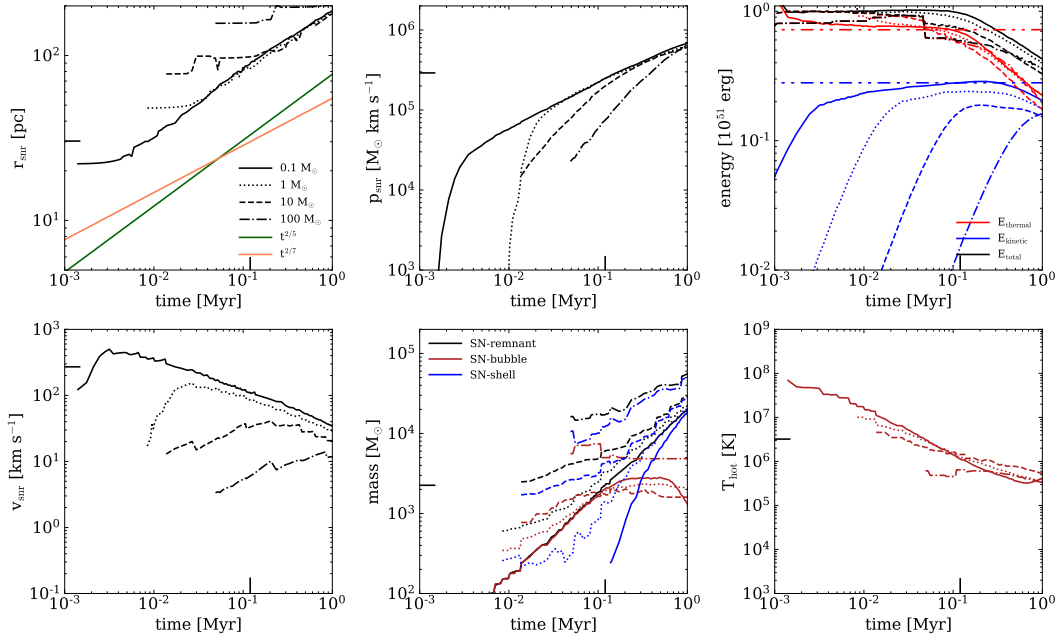


Figure A2. Same as Figure 4 for an ambient density of 0.1 cm^{-3}